J. Fluid Mech. (2022), *vol.* 932, A4, doi:10.1017/jfm.2021.955

Tempered fractional LES modeling

Mehdi Samiee[1,2], **Ali Akhavan-Safaei**[1,2] **and Mohsen Zayernouri**[1,3,†]

[1]Department of Mechanical Engineering, Michigan State University, East Lansing, MI 48824, USA

[2]Department of Computational Mathematics, Science and Engineering, Michigan State University, East Lansing, MI 48824, USA

[3]Department of Statistics and Probability, Michigan State University, East Lansing, MI 48824, USA

(Received 2 March 2021; revised 5 September 2021; accepted 22 October 2021)

The presence of non-local interactions and intermittent signals in the homogeneous isotropic turbulence grant multi-point statistical functions a key role in formulating a new generation of large-eddy simulation (LES) models of higher fidelity. We establish a tempered fractional-order modelling framework for developing non-local LES subgrid-scale models, starting from the kinetic transport. We employ a tempered Lévy-stable distribution to represent the source of turbulent effects at the kinetic level, and we rigorously show that the corresponding turbulence closure term emerges as the tempered fractional Laplacian, $(\Delta+\lambda)^{\alpha}(\cdot)$, for $\alpha \in (0, 1)$, $\alpha \neq \frac{1}{2}$ and $\lambda > 0$ in the filtered Navier–Stokes equations. Moreover, we prove the frame invariant properties of the proposed model, complying with the subgrid-scale stresses. To characterize the optimum values of model parameters and infer the enhanced efficiency of the tempered fractional subgrid-scale model, we develop a robust algorithm, involving two-point structure functions and conventional correlation coefficients. In an *a priori* statistical study, we evaluate the capabilities of the developed model in fulfilling the closed essential requirements, obtained for a weaker sense of the ideal LES model (Meneveau, *Phys. Fluids*, vol. 6, issue 2, 1994, pp. 815–833). Finally, the model undergoes the *a posteriori* analysis to ensure the numerical stability and pragmatic efficiency of the model.

Key words: turbulence modelling, computational methods, fractals

1. Introduction

With the recent notable advancements in computer technologies and, by extension, in the computational mechanics, there is a rapidly growing interest toward using large eddy simulations (LES) in a wide range of applications (Piomelli 2014; Bouffanais 2010). In LES, one resolves the large energy-containing eddies by modelling the interplay between

---

† Email address for correspondence: zayern@msu.edu

large- and subgrid-scale motions. Due to the tendency of small scales to homogeneous and universal dynamics, LES offers more accurate predictions comparing with the results of resolving the Reynolds-averaged Navier–Stokes (RANS) equations (Zhiyin 2015; Holgate *et al.* 2019). Furthermore, it lightens the burden of computational costs imposed by accurately capturing the dissipative scales in direct numerical simulations (DNS).

Concurrent with the recent computational advancements, a marked shift occurred toward using artificial intelligence (AI) as an effective and tractable tool in turbulence modellings due to their significant capabilities in reproducing statistical properties (Beck & Kurz 2020). Several assorted machine learning (ML) algorithms were proposed for turbulence closure problems including kernel regression and a deep neural network (Pawar *et al.* 2020; Sirignano, MacArt & Freund 2020; Portwood *et al.* 2021). Essentially, pure ML based approaches are limited by the representative training dataset though they appear to be simpler for implementation. Moreover, to pinpoint complex patterns, large volumes of data are required for the algorithms to learn physical constraints (e.g. frame invariance) and statistical properties, which secondarily makes further complications like optimizing of data compression (Chao *et al.* 2020). This reveals the significance of physics-based models in mentoring the AI approaches and pushing hybrid models as a new direction (Patra, Bevilacqua & Safaei 2018; Jouybari *et al.* 2020; Taghizadeh, Witherden & Girimaji 2020; Willard *et al.* 2020).

Physics-based approaches introduce a mathematical representation of physical structures through a number of parameters with a sufficient amount of information. Contrary to ML based approaches, physics-based models do not involve large volumes of data although they are inherently limited by the model incompleteness or the complexity of parameterizing physical structures (Chao *et al.* 2020). Accordingly, it is markedly essential to entail the underlying statistical properties in formulating and inferring an optimum model in a numerically rigorous framework. Employing principles of physics and borrowing insights from the statistical analysis, this approach forms a model for real phenomena, which can also be used to guide the ML algorithms properly (see, e.g. Kurz & Beck 2020; Akhavan-Safaei, Samiee & Zayernouri 2021; You *et al.* 2021).

Establishment of such a physically consistent LES model ties strongly with characterization of non-local turbulence mechanisms and a better understanding of anomalous structures. As a puzzling feature, the non-Gaussian behaviour of turbulent dynamics is linked to the spatial intermittency of small-scale motions, which is embodied in the form of very thin and elongated vortices (Vincent & Meneguzzi 1991; Laval, Dubrulle & Nazarenko 2001). Technically, the non-local closure of Navier–Stokes (NS) equations, originated from the Green's function of the Laplacian operator for solving the Poisson pressure equation, induces long-range interactions (non-local triadic structures) in spectral space of homogeneous turbulence (Sagaut & Cambon 2008). In a preliminary investigation of isotropic turbulence (She, Jackson & Orszag 1990), the significant role of highly vortical structures, typically tube-like, was disclosed on generating non-local dynamics and coherence of turbulence. Supported by Laval *et al.* (2001), non-locality as a crucial element in generating intermittent structures has a tendency to prevail the local interactions by orders of magnitude. Recently, Mishra & Girimaji (2019) studied the role of pressure on non-local mechanisms in incompressible turbulent flows and identified the intercomponent of energy transfer by the rapid pressure–strain correlation. For more information, the reader is referred to Buaria, Pumir & Bodenschatz (2020), Pang *et al.* (2020), Akhavan-Safaei, Seyedi & Zayernouri (2020) and Hamlington & Dahm (2008).

From this perspective, an ideal subgrid-scale (SGS) model represents the correct statistics of the filtered real turbulence at the resolved levels. Given the dependence of an ideal model on an infinite-dimensional set of multi-point statistics, it would be more practical to define a weaker set of conditions in a study of SGS parameterizations (Sagaut & Cambon 2008). As one of the earliest studies on statistical analysis of LES, Meneveau (1994) derived a closed set of necessary, yet mild, conditions to fulfil *a priori* consistency in SGS quantities. In the case of homogeneous anisotropic turbulent flows, the Kármán-Howarth (KH) theorem were studied in Hill (2002) by eliminating pressure velocity correlations to determine the two-point structure function equations. By proposing a hyper eddy-viscosity term in Cerutti, Meneveau & Knio (2000), SGS dissipation spectra were measured in a locally isotropic turbulence to assess the ability of classical two-point closures in predicting the mean energy transfer. More generally, Cambon & Scott (1999) discussed the importance of non-local structures in capturing the wide continuum of turbulent scales in RANS modellings. Focusing on anisotropic dynamics, Cambon & Scott (1999) and Kassinos, Reynolds & Rogers (2001) reviewed a range of non-local RANS models and described the improvements in understanding the internal dynamics of turbulent structures. Furthermore, Mishra & Girimaji (2017) outlined a framework to formulate a pressure–strain correlation model by augmenting the degree of non-locality over a range of homogeneous turbulent flows. Recently, some of the prevailed challenges in developing an optimal LES model were reviewed succinctly by Moser, Haering & Yalla (2021).

Statistical descriptions of an ideal closure model motivated us toward developing non-local approaches in terms of two-point high-order structure functions. The eddy damped quasi-normal Markovian approach, described in Briard, Gomez & Cambon (2016), undertakes closing of SGS motions in a spectral space by involving high-order statistical moments. As a functional approach, direct interaction approximation pushes the non-Markovanized stochastic models to the direction of turbulence closure problems, whose solutions are constructed in a fraction form (Shivamoggi & Tuovila 2019). Furthermore, multifractal models (Yang & Lozano-Durán 2017; Burton & Dahm 2005) suggest a potential realizable strategy to accurately capture anomalous scaling exponents, observed in turbulent velocity increments. In addressing statistical local and non-local interactions, this progress proceeds with modelling turbulent effects at the kinetic level. Premnath, Pattison & Banerjee (2009) developed a framework for applying a dynamic procedure into the lattice-Boltzmann method for LES of inhomogeneous and anisotropic turbulent flows. A new collision approach was proposed by Jacob, Malaspinas & Sagaut (2018) for LES of weakly compressible flows using two forms of the modified Bhatnagar–Gross–Krook (BGK) collision operators. For a more comprehensive review of the literature, we refer the reader to Jin *et al.* (2018) and Sagaut (2010).

Focusing on the key ideas of (i) describing of anomalous structures in turbulence and (ii) non-local closure modelling, fractional calculus appears to be a tractable mathematical tool due to their power-law or logarithmic types of kernel. Egolf & Hutter (2017) generalized Reynolds shear stresses in a local zero-equation to the fractional counterparts. Furthermore, Epps and Cushmann-Roisin derived fractional NS equations from the Boltzmann transport equation in Epps & Cushman-Roisin (2018), which supply profound understandings of turbulent non-local effects at the kinetic level. For more information, Egolf & Hutter (2020) provide a comprehensive overview of fractional and non-local turbulence, spanning from coherent structures to state-of-the-art ideas on closure modelling of canonical flows. Recently, Di Leoni *et al.* (2020) contributed in fractional LES modelling by developing a two-point correlation based model in a robust physically meaning framework.

In the class of non-local models, Samiee, Akhavan-Safaei & Zayernouri (2020*a*) laid out a mathematical framework for developing fractional models, which starts treating turbulence effects at the kinetic level. In a precise derivation, the proposed distribution function in the closed form of filtered collision operator turns into a fractional model in the LES equations. Throughout a data-driven approach, Akhavan-Safaei *et al.* (2021) extended the fractional modelling to the LES of scalar turbulence using two-point correlation functions between the SGS scalar flux and filtered scalar gradient. Inspired by the self-similar behaviour of cascading of energy in the inertial range and the exponential decay in the dissipation range, we focus on developing a tempered non-local model within the proposed fractional framework. Here, we briefly highlight the main contributions of this work as follows.

(i) We develop a tempered fractional SGS (TFSGS) model by employing a tempered heavy-tailed distribution starting from the kinetic level. Such a tractable fractional operator offers a great flexibility in characterizing non-local structures in the turbulent inertial and dissipation ranges through fractional and tempering parameters.
(ii) To achieve the enhanced performance of the proposed model, we also present an optimization algorithm, involving two-point structure functions. Regarding the best approximation of an ideal physics-based model, the optimized TFSGS model restores many essential statistical properties of SGS stresses and presents an *a priori* consistency in the dissipation spectrum.
(iii) We carry out an *a posterioi* analysis to investigate the numerical stability and performance of the TFSGS model.

The paper is organized as follows. In § 2 we introduce some preliminaries of tempered fractional calculus. We outline a mathematical framework in § 3 to develop the tempered fractional model from the Boltzmann transport equation and derive the corresponding form for SGS quantities. Within a statistical framework, we present a two-point structure based algorithm to infer the optimal behaviour of the tempered fractional model in § 4. Using the DNS database of a stationary isotropic turbulent flow, we evaluate the statistical *a priori* analysis and perform a comparative study on the two-point structure functions in § 5. Moreover, we study numerical stability of the LES solutions through an *a posteriori* investigation in § 5. Lastly, § 6 summarize the findings with a conclusion.

2. Preliminaries on tempered fractional calculus

Fractional calculus introduces well-established mathematical tools for an accurate description of anomalous phenomena, ubiquitous in a wide range of applications from bio-tissues (Ionescu *et al.* 2017; Naghibolhosseini & Long 2018) and material science (Meral, Royston & Magin 2010; Suzuki & Zayernouri 2021; Suzuki *et al.* 2021*a*) to vibration (Suzuki *et al.* 2021*b*), porous media (Xie & Fang 2019; Zaky, Hendy & Macías-Díaz 2020; Samiee *et al.* 2020*b*). As an alternative approach to standard methods, they leverage their inherent potentials in representing long-range interactions, self-similar structures, sharp peaks and memory effects in a variety of applications (see Kharazmi & Zayernouri 2019; Burkovska, Glusa & D'Elia 2020). This potential is substantially indicated by power-law or logarithmic kernels of convolution type in the corresponding fractional operators. From the stochastic point of view, fractional transport models arise from the heavy-tailed distribution functions in modelling the underlying super- or sub-diffusive motions of particles in complex heterogeneous systems at the microscopic level (Samiee, Zayernouri & Meerschaert 2019). Nevertheless, common patterns in nature follow finite-variance dynamics, which urges the role of tempered fractional calculus in representing natural cut-offs in real applications and retaining their finite statistical properties.

Recalling from Sabzikar, Meerschaert & Chen (2015) and Zayernouri, Ainsworth & Karniadakis (2015), we begin with the definitions of the left- and right-sided tempered fractional derivatives respectively as

$$\mathcal{D}^{\alpha,\lambda}_{\pm x}u(x) = \frac{\alpha}{\varGamma(1-\alpha)}\int_0^\infty \frac{u(x)-u(x\mp s)}{s^{\alpha+1}\mathrm{e}^{\lambda s}}\,\mathrm{d}s, \tag{2.1}$$

where the fractional derivative order, $\alpha \in (0,1)$, and the tempering parameter, $\lambda > 0$. Also, $\varGamma(\cdot)$ represents a Gamma function. For $\alpha \in (1,2)$, the corresponding fractional derivatives are given by

$$\mathcal{D}^{\alpha,\lambda}_{\pm x}u(x) = \frac{\alpha(\alpha-1)}{\varGamma(2-\alpha)}\int_0^\infty \frac{u(x\mp s)-u(x)\pm s\dfrac{\mathrm{d}u(x)}{\mathrm{d}x}}{s^{\alpha+1}\mathrm{e}^{\lambda s}}\,\mathrm{d}s. \tag{2.2}$$

The link between the derivatives in (2.2) and (2.3) and their counterparts in the Riemann–Liouville sense are described by

$$^{RL}\mathcal{D}^{\alpha,\lambda}_{\pm x}u(x) = \mathcal{D}^{\alpha,\lambda}_{\pm x}u(x) + \lambda^\alpha u(x), \tag{2.3}$$

$$^{RL}\mathcal{D}^{\alpha,\lambda}_{\pm x}u(x) = \mathcal{D}^{\alpha,\lambda}_{\pm x}u(x) + \lambda^\alpha u(x) \pm \alpha\lambda^{\alpha-1}\frac{\mathrm{d}u(x)}{\mathrm{d}x}. \tag{2.4}$$

In particular, for $n \geqslant 0$, the tempered integer-order derivatives are reduced as

$$^{RL}\mathcal{D}^{n,\lambda}_{+x}u(x) = \mathrm{e}^{-\lambda x}\frac{\mathrm{d}^n\left(\mathrm{e}^{\lambda x}u(x)\right)}{\mathrm{d}x^n}, \tag{2.5}$$

which recover the classic integer-order derivatives as $\lambda \to 0$.

Let $\mathcal{F}[u](\xi)$ denote the Fourier transform of u, where ξ is the Fourier numbers. Then, we obtain

$$\mathcal{F}\left[{}^{RL}\mathcal{D}^{\alpha,\lambda}_{\pm x}u(x)\right] = (\lambda \pm \mathfrak{i}\,\xi)^\alpha\,\mathcal{F}[u](\xi). \tag{2.6}$$

In this context, the corresponding Fourier transform of the left- and right-sided tempered fractional integrals are given by

$$\mathcal{F}\left[{}^{RL}\mathcal{I}^{\alpha,\lambda}_{\pm x}u(x)\right](\xi) = (\lambda \pm \mathfrak{i}\,\xi)^{-\alpha}\,\mathcal{F}[u](\xi). \tag{2.7}$$

Evidently, tempered integrals and derivatives act as an inverse operator when u possesses sufficient regularity (see Sabzikar *et al.* 2015; Zhang, Deng & Karniadakis 2018). Moreover, tempered fractional operators preserve semi-group property, which prepares a useful and rigorous framework for further numerical considerations.

2.1. *Tempered fractional Laplacian*

Denoted by $(\varDelta+\lambda)^\alpha(\cdot)$, we define the tempered fractional Laplacian of the integral form as

$$(\varDelta+\lambda)^\alpha u(\boldsymbol{x}) = C_{d,\alpha}\,\mathrm{P.V.}\int_{\mathbb{R}^d}\frac{u(\boldsymbol{x})-u(\boldsymbol{s})}{\mathrm{e}^{\lambda|\boldsymbol{x}-\boldsymbol{s}|}|\boldsymbol{x}-\boldsymbol{s}|^{2\alpha+d}}\,\mathrm{d}\boldsymbol{s}, \tag{2.8}$$

where $C_{d,\alpha} = (-\varGamma(d/2)/2\pi^{d/2}\varGamma(-2\alpha))(1/{}_2F_1(-\alpha,(d+2\alpha-1)/2;d/2;1))$ for $\alpha \in (0,1)$ and $\alpha \neq \frac{1}{2}$. In particular, $d = 1$ $(\varDelta+\lambda)^\alpha$ is reduced to the so-called *Riesz* fractional form, described by

$$
\begin{aligned}
(\varDelta+\lambda)^{\alpha}u(x) &= (-1)^{\lfloor 2\alpha\rfloor+1}\frac{{}^{RL}\mathcal{D}^{\alpha,\lambda}_{+x}u(x)+{}^{RL}\mathcal{D}^{\alpha,\lambda}_{-x}u(x)}{2}\\
&= C_{\alpha}\,\text{P.V.}\int_{\mathbb{R}}\frac{u(x)-u(s)}{\mathrm{e}^{\lambda|x-s|}|x-s|^{2\alpha+1}}\mathrm{d}s,
\end{aligned}
\tag{2.9}
$$

where $C_{\alpha}=(-\varGamma(1/2)/2\pi^{1/2}\varGamma(-2\alpha))(1/\cos(\pi\alpha))$ (see Zhang *et al.* 2018). In Appendix A, we detail the derivation of the Fourier transform of $(\varDelta+\lambda)^{\alpha}u(\boldsymbol{x})$, formulated as

$$
\begin{aligned}
&\mathcal{F}\left[(\varDelta+\lambda)^{\alpha}u(\boldsymbol{x})\right](\boldsymbol{\xi})\\
&\quad=\mathfrak{C}_{d,\alpha}\times\left(\lambda^{2\alpha}-(\lambda^{2}+\xi^{2})^{\alpha}{}_{2}F_{1}(-\alpha,\frac{d+2\alpha-1}{2};\frac{d}{2};\frac{\xi^{2}}{\xi^{2}+\lambda^{2}})\right)\mathcal{F}\left[u\right](\boldsymbol{\xi}),
\end{aligned}
\tag{2.10}
$$

in which $\mathfrak{C}_{d,\alpha}=1/{}_{2}F_{1}(-\alpha,(d+2\alpha-1)/2;d/2;1)$ and $\xi=|\boldsymbol{\xi}|$. For $d=3$, we define $\mathfrak{C}_{\alpha}=1/{}_{2}F_{1}(-\alpha,(2+2\alpha)/2;3/2;1)$. It is worth noting that when λ approaches 0, we recover the usual fractional Laplacian in both integral or Fourier forms.

3. Boltzmannian framework

The kinetic Boltzmann transport (BT) is a formal framework for describing fluid particle motions over a wide range of flow physics (e.g. rarefied gas flows and turbulence). This framework offers great potential for the statistical description of turbulent small scales towards a better understanding of coherent structures in turbulence yet at the kinetic level. As an alternative approach in turbulent closure modelling, reconciling SGS terms in the BT and the NS equations can conceivably give rise to a rigorous physics-based model at the continuum level.

Within the BT framework proposed in Samiee *et al.* (2020*a*), we develop an SGS model, respecting the statistical and physical properties of turbulent unresolved-scale motions.

3.1. *Subgrid-scale modelling*

In the description of incompressible turbulent flows, we consider LES equations (Pope 2000), governing the dynamics of the resolved-scale flow variables,

$$
\frac{\partial\bar{\boldsymbol{V}}}{\partial t}+\bar{\boldsymbol{V}}\boldsymbol{\cdot}\nabla\bar{\boldsymbol{V}}=-\frac{1}{\rho}\nabla\bar{p}+\nu\nabla\boldsymbol{\cdot}\bar{\boldsymbol{S}}-\nabla\boldsymbol{\cdot}\boldsymbol{T}^{\mathcal{R}},
\tag{3.1}
$$

where in the index form $\bar{\boldsymbol{V}}(\boldsymbol{x},t)=\bar{V}_{i}$ and $\bar{p}(\boldsymbol{x},t)$ represent the velocity and the pressure fields for $i=1,2,3$ and $\boldsymbol{x}=x_{i}$. Moreover, ν and ρ denote the kinematic viscosity and the density, respectively. Considering $\mathcal{L}$ as the filter width, the filtered field is obtained in the form of $\bar{\boldsymbol{V}}=G*\boldsymbol{V}$, where $G=G(\boldsymbol{x})$ denotes the kernel of a spatial isotropic filtering type and $*$ is the convolution operator. By implementing the filtering operation, we decompose the velocity field, $\boldsymbol{V}$, into the filtered (resolved), $\bar{\boldsymbol{V}}$, and the residual, $\boldsymbol{v}$, components. In (3.1) the filtered strain rate, $\bar{\boldsymbol{S}}$, and the SGS stress tensor, $\boldsymbol{T}^{\mathcal{R}}$, are defined by $\bar{\boldsymbol{S}}_{ij}=\frac{1}{2}(\partial V_{i}/\partial x_{j}+\partial V_{j}/\partial x_{i})$ and $\boldsymbol{T}^{\mathcal{R}}_{ij}=\overline{V_{i}V_{j}}-\bar{V}_{i}\bar{V}_{j}$.

Since the filtering operator cannot commute with the nonlinear terms in the NS equations, SGS stresses must be modelled in terms of the resolved velocity field. As a common yet reliable approach, Smagorinsky (1963) offered modelling the SGS stresses by borrowing the Boussinesq approximation from the kinetic theory such that $\boldsymbol{T}^{\mathcal{R}} = -2\nu_R \bar{\boldsymbol{S}}$ and ν_R is indicated by $\nu_R = (C_s\mathcal{L})^2 \, |\bar{\boldsymbol{S}}|$, where $|\bar{\boldsymbol{S}}| = \sqrt{2\bar{\boldsymbol{S}}_{ij}\bar{\boldsymbol{S}}_{ij}}$ and C_s is the Smagorinsky (SMG) constant.

3.2. *The BGK equation and the closure problem*

Starting from the Boltzmann kinetic theory (Soto 2016), the evolution of mass distribution function f is governed by the BT equation as

$$\frac{\partial f}{\partial t} + \boldsymbol{u} \boldsymbol{\cdot} \nabla f = \varOmega(f), \tag{3.2}$$

in which $f(t, \boldsymbol{x}, \boldsymbol{u}) \, \mathrm{d}\boldsymbol{x} \, \mathrm{d}\boldsymbol{u}$ represent the probability of finding the mass of particles, located within volume $\mathrm{d}\boldsymbol{x} \, \mathrm{d}\boldsymbol{u}$ centred on a specific location, $\boldsymbol{x}$, and speed, $\boldsymbol{u}$, at time t. It is worth noting that in the particle phase space $\boldsymbol{x}$, $\boldsymbol{u}$ and t are independent variables. Technically, the left-hand side of (3.2) concerns the streaming of non-reacting particles in the absence of any body force and the right-hand side represents the collision operator. The most common form of $\varOmega(f)$ with a single collision is the so-called BGK approximation (Soto 2016), given by

$$\varOmega(f) = -\frac{f - f^{eq}}{\tau}, \tag{3.3}$$

where τ represents the single relaxation time. In the case of incompressible flows with a roughly constant temperature, τ is assumed to be independent of macroscopic flow field velocity and pressure. Moreover, under the circumstances of thermodynamic equilibrium of particles, $f^{eq}(\varDelta)$ serves as

$$f^{eq}(\varDelta) = \frac{\rho}{U^3} F(\varDelta), \tag{3.4}$$

where $F(\varDelta) = \mathrm{e}^{-\varDelta/2}$, $\varDelta = |\boldsymbol{u} - \boldsymbol{V}|^2/U^2$ as an isotropic Maxwellian distribution and U denotes the agitation speed. More specifically, $U = \sqrt{3k_B T/m}$, in which k_B, T and m represent the Boltzmann constant, room temperature and molecular weight of air.

By recalling the basics of the BT equation from Epps & Cushman-Roisin (2018), Samiee *et al.* (2020*a*), we introduce the following quantities: L as the macroscopic length scale, l_s as the microscopic characteristic length associated with the Kolmogorov length scale, l_m as the average distance, travelled by a particle between successive collisions. Furthermore, we define $\boldsymbol{x}'$ as the location of particles before scattering, where $\boldsymbol{x}$ is the current location. Thus, $\boldsymbol{x}' = \boldsymbol{x} - (t - t')\boldsymbol{u}$, where $\boldsymbol{u}$ is assumed to be constant during $t - t'$. The analytical solution of (3.2) and (3.3) is given by

$$\begin{aligned} f(t, \boldsymbol{x}, \boldsymbol{u}) &= \int_0^\infty \mathrm{e}^{-s} f^{eq}(t - s\tau, \boldsymbol{x} - s\tau\boldsymbol{u}, \boldsymbol{u}) \, \mathrm{d}s \\ &= \int_0^\infty \mathrm{e}^{-s} f^{eq}_{s,s}(\varDelta) \, \mathrm{d}s, \end{aligned} \tag{3.5}$$

where $s \equiv (t - t')/\tau$ and $f^{eq}_{s,s}(\varDelta) = f^{eq}(t - s\tau, \boldsymbol{x} - s\tau\boldsymbol{u}, \boldsymbol{u})$.

REMARK 3.1. *In order to develop an LES model within the kinetic transport framework, we constrain our attention to the BT equation with the BGK collision approximation, involving a single relaxation time. Moreover, we follow assumption 1 in Samiee et al.*

(2020a, p. 4) in the further derivations to establish a physical connection between the collision operator and the convective terms at the continuum level.

In description of turbulence effects at the kinetic level, we decompose f into the filtered, $\bar{f}$, and residual values, f', where $\bar{f} = G * f$. As defined previously, G represents the kernel of any generic spatial isotropic filtering type. Then, the filtered kinetic transport for $\bar{f}$ suffices

$$\frac{\partial \bar{f}}{\partial t} + \boldsymbol{u}\cdot\nabla\bar{f} = -\frac{\bar{f} - \overline{f^{eq}(\varDelta)}}{\tau}, \tag{3.6}$$

in which u is independent of t and $\boldsymbol{x}$. Ensuing (3.5), the analytical solution of (3.6) is described by

$$\bar{f}(t,\boldsymbol{x},\boldsymbol{u}) = \int_0^\infty \mathrm{e}^{-s}\,\overline{f^{eq}_{s,s}(\varDelta)}\,\mathrm{d}s, \tag{3.7}$$

where $\overline{f^{eq}_{s,s}(\varDelta)} = \overline{f^{eq}(\varDelta(t-s\tau, \boldsymbol{x}-s\tau\boldsymbol{u}, \boldsymbol{u}))}$. Let define $\bar{\varDelta} := |\boldsymbol{u}-\bar{\boldsymbol{V}}|^2/U^2$. Due to the nonlinear character of the collision operator (Girimaji 2007), the filtering operation does not commute with $\varOmega$, which yields the following inequality as

$$\overline{f^{eq}(\varDelta)} = \frac{\rho}{U^3}\,\overline{\mathrm{e}^{-\varDelta/2}} \neq \frac{\rho}{U^3}\,\mathrm{e}^{-\bar{\varDelta}/2} = f^{eq}(\bar{\varDelta}). \tag{3.8}$$

This inequality gives rise to the so-called turbulence closure problem at the kinetic level. From the mathematical standpoint, the SGS motions stem from the convective nonlinear terms in the NS equations, which resembles the corresponding advective term of the BT equation. Therefore, it seems natural to recognize $\boldsymbol{u}\cdot\nabla f$ responsible for the unresolved turbulence effects in the BT equation, they manifest implicitly via the filtered collision operator though. That is, the filtered collision term on the right-hand side of (3.6) undertakes not only molecular collisions, but also the embedded SGS motions. By emphasizing on the importance of modelling $\overline{f^{eq}(\varDelta)}$ in the filtered collision operator, we review some different approaches in treating nonlinear effects.

Classical approaches. As a common practice in modelling the SGS closures, the attentions were directed toward with eddy-viscosity approximations by employing a modified relaxation time, $\tau^\star$, in the BT equation (e.g. Sagaut 2010). Therefore, the proposed filtered BT equation reads as

$$\frac{\partial \bar{f}}{\partial t} + \boldsymbol{u}\cdot\nabla\bar{f} = -\frac{\bar{f} - f^{eq}(\bar{\varDelta})}{\tau^\star}. \tag{3.9}$$

In this approach, the inequality in (3.8) is disregarded through using $\tau^\star$, which renders the SGS model inappropriate for reproducing many features of the SGS motions. Nevertheless, there some non-eddy-viscosity models within the lattice Boltzmann framework, which make use of (3.8) to propose a more consistent SGS model. For more details, the reader is referred to Chen *et al.* (2004), Premnath *et al.* (2009) and Malaspinas & Sagaut (2012).

Fractional approach. In the proposed framework in Samiee *et al.* (2020*a*), the modelling of turbulence nonlinear effects begins with closing the filtered collision operator, where the multi-exponential behaviour of $\overline{f^{eq}(\varDelta)}$ is approximated properly by a heavy-tailed distribution function. Therefore, the $\overline{f^{eq}(\varDelta)}$ in (3.6) is described by

$$\overline{f^{eq}(\varDelta)} - f^{eq}(\bar{\varDelta}) \simeq f^{\beta}(\bar{\varDelta}), \tag{3.10}$$

where $f^{\beta}(\bar{\varDelta}) = (\rho/U^3)F^{\beta}(\varDelta)$ and $F^{\beta}(\varDelta)$ denotes an isotropic Lévy β-stable distribution. By taking the first moment of (3.6), one derives the corresponding fractional Laplacian operator, termed as fractional SGS (FSGS) model, at the continuum level, where

$$(\nabla \cdot \boldsymbol{T}^R) = \mu_\alpha (-\Delta)^\alpha \bar{V}, \tag{3.11}$$

where $\mu_\alpha = (\rho(U\tau)^{2\alpha}\Gamma(2\alpha+1)/\tau)\,(2^{2\alpha}\Gamma(\alpha+d/2)/\pi^{d/2}\Gamma(-\alpha))\,c_\alpha$ for $\alpha \in (0,1)$ and c_α is a real-valued constant. In principle, the choice of distribution function in (3.10) gives rise to a non-local operator of the resolved flow field in (3.1) as an SGS model.

Despite the notable potentials of the FSGS model in maintaining some important physical and mathematical properties of the SGS stresses, it lacks a finite second-order statistical moment. To control this statistical barrier in the FSGS model and to achieve more congruence between both sides of (3.10), we seek a finite-variance alternative for the Lévy β-stable distribution by employing the tempered counterpart and thereby a more flexible and predictive fractional operator in the LES equations in the following subsection.

3.3. *Tempered fractional SGS modelling*

Multi-exponential functions express a power-law behaviour in the moderate range of distribution and eventually relaxes into an exponential decay (see Evin *et al.* 2016). By engaging more exponential terms to a multi-exponential function, the corresponding power-law behaviour extends toward long ranges; however, it is bound to vanish exponentially at the tail of the distribution, which is enforced by the nature of the physical phenomenon. As a rich class of stochastic functions for fitting into realistic phenomena, tempered stable distributions (Sabzikar *et al.* 2015) resemble a shear power law at the moderate range and then converge to an exponential decay.

Inspired by this argument, we propose to model $\overline{f^{eq}(\varDelta)}$ with a coefficient of tempered Lévy β-stable distribution, denoted by $f^{\beta,\lambda}(\bar{\varDelta})$, within the proposed fractional framework as

$$\overline{f^{eq}(\varDelta)} - f^{eq}(\bar{\varDelta}) \simeq f^{Model}(\bar{\varDelta}) = c_{\beta,\lambda} f^{\beta,\lambda}(\bar{\varDelta}), \tag{3.12}$$

where $c_{\beta,\lambda}$ is a real-valued constant number. Moreover, we consider $\beta \in (-1-d/2, -d/2)$, $\lambda > 0$ and $d = 3$ represents the dimension of the physical domain. Therefore, the filtered BT equation reads as

$$\begin{aligned}\frac{\partial \bar{f}}{\partial t} + \boldsymbol{u} \cdot \nabla \bar{f} &= -\frac{\bar{f} - f^{eq}(\bar{\varDelta}) + f^{eq}(\bar{\varDelta}) - \overline{f^{eq}(\varDelta)}}{\tau} \\ &\simeq -\frac{\bar{f} - f^{eq}(\bar{\varDelta}) - f^{Model}(\bar{\varDelta})}{\tau}.\end{aligned} \tag{3.13}$$

For the sake of simplicity, we take $f^*(\bar{\varDelta}) = f^{eq}(\bar{\varDelta}) + f^{Model}(\bar{\varDelta})$. The approximation in (3.13) conceivably provides a good fit into the filtered collision operator by maintaining the significant statistical features of $\overline{f^{eq}(\varDelta)}$ and sets a physically richer starting point for developing a more expressive non-local LES model at the continuum level. It should be noted that β and λ rely not only on the thermodynamic properties and boundary conditions, but also they are functions of the flow Reynolds number and the filter width, $\mathcal{L}$. In following sections we assume that the Reynolds number has a relatively constant value in the stationary turbulent flow to reduce fractional parameters as a function of $\mathcal{L}$.

In this regard, the macroscopic variables associated with the flow field can be reconstructed according to

$$\bar{\rho} = \int_{\mathbb{R}^d} \bar{f}(t, \boldsymbol{x}, \boldsymbol{u})\, \mathrm{d}\boldsymbol{u}, \tag{3.14}$$

$$\bar{V}_i = \frac{1}{\rho} \int_{\mathbb{R}^d} u_i \bar{f}(t, \boldsymbol{x}, \boldsymbol{u})\, \mathrm{d}\boldsymbol{u}, \quad i = 1, 2, 3, \tag{3.15}$$

where $\bar{\rho} = \rho$ for an incompressible flow. To establish the connection between the kinetic description and the filtered NS equation, we proceed with deriving the macroscopic form of (3.13) by multiplying it with $\boldsymbol{u}$, and integrating over the kinetic momentum, which yields

$$\int_{\mathbb{R}^d} \left(\boldsymbol{u} \frac{\partial \bar{f}}{\partial t} + \nabla \boldsymbol{\cdot} (\boldsymbol{u}^2 \bar{f}) \right) \mathrm{d}\boldsymbol{u} = 0 \quad \Longrightarrow \quad \rho \frac{\partial \bar{\boldsymbol{V}}}{\partial t} + \nabla \boldsymbol{\cdot} \int_{\mathbb{R}^d} \boldsymbol{u}^2 \bar{f}\, \mathrm{d}\boldsymbol{u} = 0. \tag{3.16}$$

Recalling the assumptions in remark 3.1 that $\int_{\mathbb{R}^d} \boldsymbol{u}((\bar{f} - f^*(\bar{\Delta}))/\tau)\, \mathrm{d}\boldsymbol{u} = 0$ due to microscopic reversibility of particle collisions. Following the derivations in Samiee *et al.* (2020*a*, pp. 5–6), we add and subtract $\bar{\boldsymbol{V}}\bar{\boldsymbol{V}}$ to the advection term and accordingly, (3.16) is found to be

$$\rho \left(\frac{\partial \bar{\boldsymbol{V}}}{\partial t} + \nabla \boldsymbol{\cdot} \bar{\boldsymbol{V}}\bar{\boldsymbol{V}} \right) = -\nabla \boldsymbol{\cdot} \varsigma, \tag{3.17}$$

where ς in the index form is expressed as

$$\varsigma_{ij} = \int_{\mathbb{R}^d} (u_i - \bar{V}_i)(u_j - \bar{V}_j) \bar{f}\, \mathrm{d}\boldsymbol{u}. \tag{3.18}$$

Comparing (3.1) and (3.17), it turns out that the pressure term, viscous and SGS stresses all trace back to $\nabla \boldsymbol{\cdot} \varsigma$, where $\varsigma_{ij} = -\bar{p}\,\delta_{ij} + \boldsymbol{\mathsf{T}}_{ij}^{shear} + \boldsymbol{\mathsf{T}}_{ij}^{\mathcal{R}}$. By plugging (3.7) into the kinetic definitions of each term in ς_{ij}, we obtain

$$\bar{p}\,\delta_{ij} = -\int_{\mathbb{R}^d} (u_i - \bar{V}_i)(u_j - \bar{V}_j) f^*(\bar{\Delta})\, \mathrm{d}\boldsymbol{u} \int_0^\infty \mathrm{e}^{-s}\, \mathrm{d}s, \tag{3.19}$$

$$\boldsymbol{\mathsf{T}}_{ij}^{shear} = \int_0^\infty \int_{\mathbb{R}^d} (u_i - \bar{V}_i)(u_j - \bar{V}_j) \times \left(f_{s,s}^{eq}(\bar{\Delta}) - f^{eq}(\bar{\Delta}) \right) \mathrm{e}^{-s}\, \mathrm{d}\boldsymbol{u}\, \mathrm{d}s = 2\mu \bar{\boldsymbol{\mathsf{S}}}_{ij}, \tag{3.20}$$

where $\mu = \rho U^2 \tau$. Similarly, by employing f^{Model} in (3.12), we attain

$$\begin{aligned} \boldsymbol{\mathsf{T}}_{ij}^{R} &= c_{\beta,\lambda} \int_0^\infty \int_{\mathbb{R}^d} (u_i - \bar{V}_i)(u_j - \bar{V}_j) \left(f_{s,s}^{\beta,\lambda}(\bar{\Delta}) - f^{\beta,\lambda}(\bar{\Delta}) \right) \mathrm{e}^{-s}\, \mathrm{d}\boldsymbol{u}\, \mathrm{d}s \\ &= \frac{\rho c_{\beta,\lambda}}{U^3} \int_0^\infty \int_{\mathbb{R}^d} (u_i - \bar{V}_i)(u_j - \bar{V}_j) \left(F^{\beta,\lambda}(\bar{\Delta}_{s,s}) - F^{\beta,\lambda}(\bar{\Delta}) \right) \mathrm{e}^{-s}\, \mathrm{d}\boldsymbol{u}\, \mathrm{d}s, \end{aligned} \tag{3.21}$$

in which $\bar{\Delta}_{s,s} = \bar{\Delta}(t - s\tau, \boldsymbol{x} - s\tau\boldsymbol{u}, \boldsymbol{u})$. As discussed in Samiee *et al.* (2020*a*, appendix), the temporal shift can be detached from $f_{s,s}^{\beta,\lambda}(\bar{\Delta})$ and then $\bar{\Delta}_{s,s}$ is simplified to $\bar{\Delta}_s = \bar{\Delta}(t, \boldsymbol{x} - s\tau\boldsymbol{u}, \boldsymbol{u})$. Therefore,

$$\boldsymbol{\mathsf{T}}_{ij}^{R} = \frac{\rho c_{\beta,\lambda}}{U^3} \int_0^\infty \int_{\mathbb{R}^d} (u_i - \bar{V}_i)(u_j - \bar{V}_j) \left(F^{\beta,\lambda}(\bar{\Delta}_s) - F^{\beta,\lambda}(\bar{\Delta}) \right) \mathrm{e}^{-s}\, \mathrm{d}\boldsymbol{u}\, \mathrm{d}s. \tag{3.22}$$

The strategy to evaluate $\boldsymbol{\mathsf{T}}_{ij}^{R}$ is to decouple the particle speed into time and displacement by employing $\boldsymbol{u} = (\boldsymbol{x}' - \boldsymbol{x})/s\tau$ and approximate the asymptotic behaviour of $F^{\beta,\lambda}(\bar{\Delta})$ with a tempered power-law distribution. In a detailed discussion in Appendix B, we show that

$$\boldsymbol{T}^{R}_{ij} = c_{\alpha,\lambda}\,\bar{\nu}_{\alpha} \sum_{k=0}^{\mathcal{K}} \bar{\phi}^{\mathcal{K}}_{k}(\alpha) \int_{\mathbb{R}^d} (x_i - x'_i)\,(x_j - x'_j) \frac{(\boldsymbol{x}-\boldsymbol{x}')\boldsymbol{\cdot}(\bar{\boldsymbol{V}}-\bar{\boldsymbol{V}}')}{|\boldsymbol{x}-\boldsymbol{x}'|^{2\alpha+5}\,\mathrm{e}^{\bar{\lambda}_k|\boldsymbol{x}-\boldsymbol{x}'|}} \mathrm{d}\boldsymbol{x}', \tag{3.23}$$

in which $\bar{\nu}_{\alpha} = (2\alpha+3)(\rho C_{\alpha}\tau^{2\alpha-1}U^{2\alpha})$ for $\alpha \in (0, \frac{1}{2}) \cup (\frac{1}{2}, 1)$ and recalling $\bar{\lambda}_k = (k/\tau U)\lambda$. Moreover, $\bar{\phi}^{\mathcal{K}}_{k}(\alpha)$ is indicated in (B9). Eventually, we disclose the integral form of $\nabla\boldsymbol{\cdot}\boldsymbol{T}^{\mathcal{R}}$ as

$$(\nabla\boldsymbol{\cdot}\boldsymbol{T}^{\mathcal{R}})_j = c_{\alpha,\lambda}\,\bar{\nu}_{\alpha} \sum_{k=0}^{\mathcal{K}} \frac{(2\alpha+\bar{\lambda}_k)}{(2\alpha+3)} \bar{\phi}^{\mathcal{K}}_{k}(\alpha) \int_{\mathbb{R}^d} \frac{(\bar{V}_j - \bar{V}'_j)}{|\boldsymbol{x}-\boldsymbol{x}'|^{2\alpha+3}\,\mathrm{e}^{\bar{\lambda}_k|\boldsymbol{x}-\boldsymbol{x}'|}} \mathrm{d}\boldsymbol{x}', \tag{3.24}$$

where $\nu_{\alpha} = c_{\alpha,\lambda}\bar{\nu}_{\alpha}$. Recalling the integral representation of a tempered fractional Laplacian in (2.8), we formulate the divergence of the SGS stresses as

$$(\nabla\boldsymbol{\cdot}\boldsymbol{T}^{\mathcal{R}})_j = \nu_{\alpha} \sum_{k=0}^{\mathcal{K}} \phi^{\mathcal{K}}_{k}(\alpha,\lambda)(\Delta+\bar{\lambda}_k)^{\alpha}\bar{V}_j, \tag{3.25}$$

where $\phi^{\mathcal{K}}_{k}(\alpha,\lambda) = ((2\alpha+\bar{\lambda}_k)/(2\alpha+3))\bar{\phi}^{\mathcal{K}}_{k}(\alpha)$. Evidently, by setting $\mathcal{K}=0$, we find that $\bar{\phi}^{\mathcal{K}}_{k}(\alpha) = \varGamma(2\alpha)$ and the new operator in (3.25) reduces to a fractional Laplacian, which recovers the FSGS model.

REMARK 3.2. *In terms of the explicit Fourier form of the tempered operator,* $(\Delta+\bar{\lambda})^{\alpha}(\cdot)$, *the TFSGS model maintains the high-order accuracy of scheme in LES solutions similar to the eddy-viscosity models without including any computational cost.*

Inferring from (3.25), our choice in the kinetic description of turbulent effects reflects in the form of a tempered fractional operator through a rigorous connection between the filtered BT and the filtered NS equations. More specifically, we adopt $\mathcal{K}=1$ and, hence, the TFSGS model can be formulated as

$$\nabla\boldsymbol{\cdot}\boldsymbol{T}^{\mathcal{R}} = \nu_{\alpha}\left[\phi^{1}_{0}(\alpha)\left(-(-\Delta)^{\alpha}\right)\bar{\boldsymbol{V}} + \phi^{1}_{1}(\alpha)\left(\Delta+\bar{\lambda}_1\right)^{\alpha}\bar{\boldsymbol{V}}\right], \tag{3.26}$$

where $\phi^{1}_{0}(\alpha) = (1/(2\alpha+3))(\varGamma(2\alpha+1)-\varGamma(2\alpha))$ and $\phi^{1}_{1}(\alpha,\lambda) = ((2\alpha+\lambda)/(2\alpha+3))\,\varGamma(2\alpha-1)$. Accordingly, the governing LES equations read as

$$\frac{\partial\bar{V}_i}{\partial t} + \frac{\partial\bar{V}_i\bar{V}_j}{\partial x_j} = -\frac{1}{\rho}\frac{\partial\bar{p}}{\partial x_i} + \nu\,\Delta\bar{V}_i - \nu_{\alpha}\sum_{k=0}^{1}\phi^{1}_{k}(\alpha,\lambda)(\Delta+\bar{\lambda}_k)^{\alpha}\,\bar{V}_i, \tag{3.27}$$

where $\alpha \in (0, \frac{1}{2}) \cup (\frac{1}{2}, 1)$, $\lambda > 0$ and $\nu_{\alpha} = \mu_{\alpha}/\rho$.

REMARK 3.3. *As a generator of tempered Lévy-stable processes, the tempered fractional Laplacian is proven to be rotationally and Galilean invariant (see Huang 2015; Kaleta & Sztonyk 2015; Cairoli 2016). Therefore, by having* ν_{α} *and* ϕ^{1}_{k} *as real-valued functions of* α *and* λ, *the TFSGS model also adopts the frame invariance property in a consistent fashion with the SGS stresses.*

3.4. *TFSGS formulations for the SGS stresses*

To study the key role of tempering fractional operators in recovering turbulent statistical structures, it is essential to establish a straightforward form of the modelled SGS stresses. Due to some numerical complications in evaluating the integral in (3.24), we settle to proceed with the Fourier representation of the TFSGS model. Employing the definition of $\mathcal{I}^\alpha$ (α-Riesz potential) from Stein (1970), it is possible to verify that

$$\nabla\cdot \boldsymbol{T}^R = (\varDelta+\lambda)^\alpha \bar{\boldsymbol{V}} = \nabla\cdot\nabla \mathcal{I}^{\alpha=1}\left[\nu_\alpha \sum_{k=0}^{1}\phi_k^1(\alpha,\lambda)(\varDelta+\bar{\lambda}_k)^\alpha \bar{\boldsymbol{V}}\right]. \tag{3.28}$$

Inspired by (3.28), we introduce $\mathcal{R}_j^{\alpha,\lambda}(\boldsymbol{\cdot}) = \nabla_j \mathcal{I}^{\alpha=1}(\varDelta+\lambda)^\alpha(\boldsymbol{\cdot})$ as a tempered fractional operator such that

$$\boldsymbol{T}_{ij}^R = \frac{\nu_\alpha}{2}\sum_{k=0}^{1}\phi_k^1(\alpha,\lambda)\left[\mathcal{R}_j^{\alpha,\bar{\lambda}_k}\bar{V}_i + \mathcal{R}_i^{\alpha,\bar{\lambda}_k}\bar{V}_j\right], \tag{3.29}$$

where $\mathcal{F}[I^{\alpha=1}] = 1/\xi^2$ and $\mathcal{F}[\nabla_j](\boldsymbol{\xi}) = -\mathfrak{i}\,\xi_j$ and $\mathfrak{i}$ denotes an imaginary unite. Following (2.10) into (3.29), we find the Fourier form of $\mathcal{R}_j^{\alpha,\lambda}$ as

$$\mathcal{F}\left[\mathcal{R}_j^{\alpha,\lambda}\right](\boldsymbol{\xi}) = \mathfrak{C}_\alpha \frac{-\mathfrak{i}\,\xi_j}{\xi^2}\left(\lambda^{2\alpha} - (\lambda^2+\xi^2)^\alpha\, {}_2F_1\left(-\alpha, 1+\alpha; \frac{3}{2}; \frac{\xi^2}{\xi^2+\lambda^2}\right)\right). \tag{3.30}$$

4. Statistical analysis

In pursuit of an ideal SGS model, nonlinearity induced by the convective terms and non-locality imparted by the pressure term in the NS equations contribute to a synthetic hierarchy of transport equations and multi-point descriptions of SGS terms, as shown in Sagaut & Cambon (2008). The infinitely extended hierarchical triangle of nonlinearity and non-locality brings up the idea of indicating a set of weaker, and yet significant, statistical conditions and makes the ideal LES model more attainable, as endorsed by Moser *et al.* (2021). To identify such statistical features, Meneveau (1994) developed a rigorous framework via a statistical *a priori* analysis and formulated some sufficient conditions for the assessment of LES models. As one of the candidates for evaluating SGS models, we give a brief review of the argued formulations in Meneveau (1994) and introduce an optimization strategy, which enables the TFSGS model to correctly generate the requisite statistical conditions.

Hereafter, we consider the following notations in study of the SGS fields. Let $\boldsymbol{T}^{R,D}$ and $\boldsymbol{T}^{R,*}$ denote the SGS stresses, implied by the true DNS data and the SGS model, respectively. We also take $\boldsymbol{r}$ as the displacement vector between two points in the correlation functions Then, $r = |\boldsymbol{r}|$. As discussed in Meneveau (1994), performing an ensemble average of the filtered NS equations offers a set of necessary conditions for an LES simulation to ensure the equality of mean velocity profiles and the second-order moments, listed as

(a) $\langle \boldsymbol{T}_{ij}^{R,D}\rangle = \langle \boldsymbol{T}_{ij}^{R,*}\rangle$,
(b) $\langle \bar{V}_i \boldsymbol{T}_{ij}^{R,D}\rangle = \langle \bar{V}_i \boldsymbol{T}_{ij}^{R,*}\rangle$,
(c) $\langle \bar{\boldsymbol{S}}_{ij} \boldsymbol{T}_{ij}^{R,D}\rangle = \langle \bar{\boldsymbol{S}}_{ij} \boldsymbol{T}_{ij}^{R,*}\rangle$,

in which conditions (*b*) and (*c*) are inferred from the ensemble-averaged SGS transport equation.

Focusing on the non-locality axis of the closure triangle for a homogeneous isotropic turbulent (HIT) flow, one obtains the so-called KH equation as

$$\left[\frac{\partial}{\partial t}-2\nu\left(\frac{\partial^2}{\partial r^2}+\frac{4}{r}\frac{\partial}{\partial r}\right)\right]B_{LL}(r,t)-\left(\frac{\partial}{\partial r}+\frac{4}{r}\right)B_{LLL}(r,t)=\left(\frac{\partial}{\partial r}+\frac{4}{r}\right)G_{LLL}(r,t) \tag{4.1}$$

for sufficiently large $\mathcal{L}\gg\eta$, where L represents the longitudinal direction. Additionally, we denote by $B_{LL}(r,t)=\langle\bar{V}_L(\boldsymbol{x},t)\,\bar{V}_L(\boldsymbol{x}+\boldsymbol{r},t)\rangle$ and $B_{LLL}(r,t)=\langle[\bar{V}_L(\boldsymbol{x},t)]^2\bar{V}_L(\boldsymbol{x}+\boldsymbol{r},t)\rangle$ the second- and third-order velocity correlation functions, respectively, and $G_{LLL}(r,t)=\langle\boldsymbol{T}^R_{LL}(\boldsymbol{x},t)\bar{V}_L(\boldsymbol{x}+\boldsymbol{r},t)\rangle$ refers to the stress–strain correlation function. Technically, the third-order correlation function in (4.1) is subdivided into B_{LLL} stemming from the resolved velocity field and $G_{LLL}(r,t)$ coming from the SGS stresses. It turns out from (4.1) that the SGS model should undergo a correct prediction of $G_{LLL}(r,t)$ to regenerate B_{LL} and B_{LLL} accurately. Referring to Meneveau (1994, pp. 819–820), we arrive at the equation

$$\left\langle[\bar{V}_L(\boldsymbol{x}+\boldsymbol{r},t)-\bar{V}_L(\boldsymbol{x},t)]^3\right\rangle+6\,G_{LLL}(r,t)=6\left\langle\bar{\boldsymbol{\mathsf{S}}}_{LL}\boldsymbol{T}^R_{LL}\right\rangle r, \tag{4.2}$$

which exhibits the only sufficient condition for modelling third-order structure in a HIT flow. Therefore, by satisfying the equality of SGS dissipation via conditions (*c*), modelling G_{LLL} remains the only requisite for capturing the third-order structure functions.

This finding reveals the significance of condition (*c*), which intrinsically ties with the stress–strain correlation function, represented by $D_{LL}(r,t)=\langle\bar{\boldsymbol{\mathsf{S}}}_{LL}(\boldsymbol{x}+\boldsymbol{r}\boldsymbol{\cdot}\boldsymbol{e},t)\boldsymbol{T}^R_{LL}\rangle$. Using the conversation in Cerutti *et al.* (2000, p. 317), D_{LL} is derived in terms of G_{LLL} as

$$D_{LL}(r,t)=\frac{7}{2}\frac{\mathrm{d}G_{LLL}(r,t)}{\mathrm{d}r}+\frac{4G_{LLL}(r,t)}{r}+\frac{r}{2}\frac{\mathrm{d}^2G_{LLL}(r,t)}{\mathrm{d}r^2}. \tag{4.3}$$

Emphasizing the role of tempering parameter in modulating the turbulent dissipation range, we therefore adopt $D_{LL}(r,t)$ as a key quantity in optimizing the TFSGS model to address condition (*c*) and capture the non-local structures in (4.2). It must be noted that in evaluating the aforementioned conditions and high-order structures, $\boldsymbol{T}^R$ represents either $\boldsymbol{T}^{R,D}$, obtained by filtering the instant DNS database, or $\boldsymbol{T}^{R,*}$, implied by implementing any model to the true resolved velocity field.

4.1. *Optimization strategy*

Devising a robust optimization framework is an inevitable element in predictive fractional and tempered fractional modellings (see Burkovska *et al.* 2020; Pang *et al.* 2020). Regarding the given set of conditions for the closure problem, we find conditions (*a*) and (*c*) practically crucial in developing an approach for estimating the parameters and coefficient associated with the TFSGS model while condition (*b*) can be substantially recovered by imposing (4.2), where $G_{LLL}(r,t)|_{r=0}=\langle\bar{V}_i\boldsymbol{T}^R_{ij}\rangle$. As we learn from the one-point correlation analysis in Samiee *et al.* (2020*a*) and the following section, correlations between the SGS stresses, obtained by the DNS data and the model, highly rely on α and λ in the TFSGS model rather than playing a central role in capturing the SGS dissipation energy and non-local structure functions. This approach provides the basis for an optimal estimation of the fractional exponents (α and λ) by employing the normalized D_{LL} and ϱ_i, defined in algorithm 1.

Algorithm 1 Estimation of the optimal model parameters for a specific $\mathcal{L}$

```
INPUT:    $\bar{V}_i,\ T^{R,D}_{ij},\ \bar{V}_L(\boldsymbol{x} + \boldsymbol{r}\cdot\boldsymbol{e}, t)$
OUTPUT:   $\alpha^{opt},\ \lambda^{opt},\ \mathrm{c}_{\alpha,\lambda}$
PROCESS:
1. Find $\alpha^{opt}$ where the maximum of $\varrho_{ii} = \left\langle \varrho\left[\mathrm{T}^{R,D}_{ii},\ \mathrm{T}^{R,TF}_{ii}\right]\right\rangle$ occurs.
2. Find $\lambda^{opt}$ where $\left[\frac{D_{LL}(r,t)}{D_{LL}(0,t)}\right]^{TF}$ fits into $\left[\frac{D_{LL}(r,t)}{D_{LL}(0,t)}\right]^{D}$ for the inferred fixed $\alpha^{opt}$.
3. Quantify the model constant such that $\mathrm{c}_{\alpha,\lambda} = \frac{\langle \bar{\boldsymbol{S}}_{ij}\boldsymbol{T}^{R,D}_{ij}\rangle}{\langle \bar{\boldsymbol{S}}_{ij}\boldsymbol{T}^{R,N}_{ij}\rangle}$, given $\alpha^{opt}$ and $\lambda^{opt}$.
VALIDATION ANALYSIS:
1. Evaluate $G_{LLL}(r)$ for the modelled and true SGS stresses to check if (4.2) is validated.
2. Perform a comparative study on the probability density functions of $\langle \bar{\boldsymbol{S}}_{ij}\boldsymbol{T}^{R}_{ij}\rangle$ and $\langle \boldsymbol{T}^{R}_{ii}\rangle$.
```

By fixing the values of fractional exponents, it is possible to accurately quantify the model coefficient and thereby reproduce the third-order structure in (4.2) via modelling G_{LLL}. In algorithm 1 we schematically present the proposed method for optimizing the parameters associated with the TFSGS model at a given flow Reynolds number (*Re*) and a specific filter width, $\mathcal{L}$.

It must be noted that in step 3, we define

$$\boldsymbol{T}^{R,N}_{ij} = \frac{\boldsymbol{T}^{R,TF}_{ij}}{\mathrm{c}_{\alpha,\lambda}} = \frac{\bar{\nu}_\alpha}{2}\sum_{k=0}^{1}\phi^1_k(\alpha,\lambda)\left[\mathcal{R}^{\alpha,\bar{\lambda}_k}_j\bar{V}_i + \mathcal{R}^{\alpha,\bar{\lambda}_k}_i\bar{V}_j\right]. \tag{4.4}$$

Moreover, superscripts '*D*' and '*TF*' represent the values obtained by filtering the true DNS data and the TFSGS model, respectively.

5. *A priori/posteriori* analyses

To attain the optimal behaviour of the TFSGS model, we follow the steps in algorithm 1 by performing an *a priori* analysis and evaluate the capabilities of the TFSGS model in generating the statistical features of turbulent flows.

5.1. *Direct numerical simulation database and LES platform*

In terms of *a priori* tests, we conduct the numerical simulation of a forced HIT flow employing the open-source pseudo-spectral NS solver for a triply periodic domain, the code of which is presented at Akhavan-Safaei & Zayernouri (2020) and the references therein (e.g. Mortensen & Langtangen 2016). It should be noted that in the next section, the LES solver is successfully prepared using this DNS code and the statistically stationary DNS dataset presented here is filtered and used as the initial conditions for the final *a posteriori* assessments.

Using the NS solver, we performed DNS of a stationary HIT flow with 320^3 resolution for a periodic computation domain as $\varOmega = [0, 2\pi]^3$ and the large-scale forcing occurs at $0 < |\boldsymbol{\xi}| \leqslant 2$ to maintain turbulence statistics stationary. Here, $\boldsymbol{\xi}$ represents the vector of Fourier wave numbers and $\xi_{max} = \sqrt{2}N/3$ is the maximum wave number solved

Re_λ	u'_{rms} (m s^{-1})	E_{tot} (m^2 s^{-2})	ν (m^2 s^{-1})	ε (m^2 s^{-3})	$\tau_{\mathscr{L}}$ (s)	Skewness	Kurtosis
190	0.67	0.68	0.001	0.1	4.2	−0.5	6.5

Table 1. Flow parameters and statistical properties in the DNS of a forced HIT flow.

numerically, where $N = 320$ is the number of grid points. In this case, $\xi_{max}\,\eta_k = 1.6 > 1$ certifies that all the scales of motion are well resolved, where η_k refers to the Kolmogorov length scale. We detail the flow parameters and some of the statistical properties in table 1, in which ε and E_{tot} denote the expected values of dissipation rate and turbulent kinetic energy, respectively. Moreover, $Re_\lambda = \frac{u'_{rms}\, l_\lambda}{\nu}$ and $l_\lambda = \sqrt{15\nu\, u'^2_{rms}/\varepsilon}$ represent the Taylor Reynolds number and micro-scale length, respectively, where $u'_{rms} = \sqrt{2E_{tot}/3}$. The simulation undergoes running for 30 eddy turnover times, $\tau_{\mathscr{L}}$, to construct 40 sample snapshots as our database. Due to the present homogeneity and isotropy in the HIT flow, we find the database adequate for obtaining the required statistics in the further analysis. The kurtosis and skewness values of the diagonal components of velocity gradient tensor are also presented in table 1, supporting non-Gaussianity of turbulent structures.

For the purpose of crunching a heavy DNS database in the statistical analysis, we develop an LES platform in Python with a focus on efficiency in obtaining two-point correlations and the ease of dealing with the fractional operators. This platform consists of three chief components: filtering the DNS database, implementation of LES models and optimization, and executing the final analysis. To overcome the burden of a timely filtering process especially in two-point correlation analysis, we introduce the scalable multi-threaded filtering code using Numpy, threading and astropy.convolution packages. Further steps in finding the optimum model parameters and applying the Fourier form of the fractional models are developed by employing the highly efficient Intelő MKL library. For more information, the reader is referred to Samiee (2021).

5.2. *Optimal estimation of fractional parameters*

In order to optimize the efficiency of the TFSGS model, we developed a flexible and rigorous strategy in algorithm 1. The proposed algorithm is equipped with verification and validation mechanisms through the conventional correlation coefficients and two-point structure functions. Recalling from § 4.1 that $\boldsymbol{T}^{R,D}_{ij}$ denotes the true SGS stresses obtained by filtering the well-resolved DNS data. Moreover, $\boldsymbol{T}^{R,*}_{ij}$ represents the general form of modelled SGS values, where $*$ can be replaced by *TF* or *SM* in the TFSGS or SMG models, respectively.

The first step in algorithm 1 concerns detecting the optimum value of the fractional exponent, α^{opt}, where the maximum of ensemble-averaged correlation between $\boldsymbol{T}^{R,D}_{ii}$ and $\boldsymbol{T}^{R,TF}_{ii}$, denoted by ϱ_{ii}, occurs. Endorsed by the results of table 2, the tempering parameter, λ, appears not to make any noticeable change in ϱ_{ii}, namely less than 3%. Therefore, we plot the variations of ϱ_{ii} vs α^{opt} in figure 1 for $i = 1, 2, 3$ in the absence of λ, where each dashed box specifies the interval of α yielding the maximum of ϱ_{ii}. Without any loss of accuracy, we adopt $\alpha^{opt} = 0.76, 0.58, 0.51$ as the corresponding minimum value in each

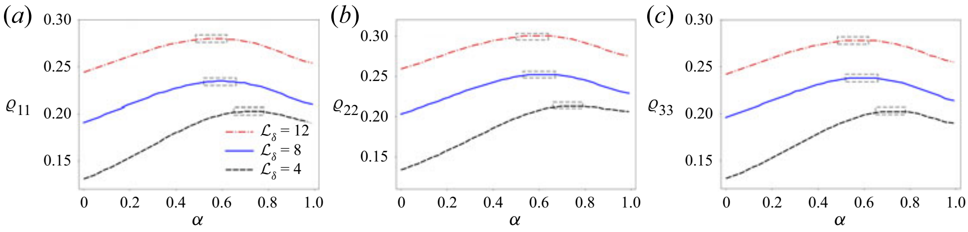

Figure 1. Variation of the correlation coefficients (*a*) ϱ_{11}, (*b*) ϱ_{22} and (*c*) ϱ_{33} vs $\alpha \in (0, 1)$ for $\mathcal{L}_\delta = 4, 8, 12$ by setting $\lambda \simeq 0$ in (4.4). The maximum values lie in the dashed boxes.

	$\mathcal{L}_\delta = 4$				$\mathcal{L}_\delta = 8$				$\mathcal{L}_\delta = 12$			
	FSGS	TFSGS		SMG	FSGS	TFSGS		SMG	FSGS	TFSGS		SMG
λ	0	0.1	4	–	0	0.35	5	–	0	0.45	5	–
ϱ_{11}	0.21	0.20	0.19	0.20	0.23	0.24	0.22	0.22	0.29	0.28	0.26	0.26
ϱ_{22}	0.21	0.20	0.20	0.21	0.24	0.24	0.23	0.23	0.29	0.28	0.26	0.26
ϱ_{33}	0.22	0.21	0.21	0.21	0.25	0.25	0.24	0.23	0.30	0.30	0.29	0.28

Table 2. The ensemble-averaged correlation coefficients (ϱ_{ii}) between SGS stresses obtained by the filtered DNS data ($\boldsymbol{T}_{ii}^{R,D}$) and the TFSGS model ($\boldsymbol{T}_{ii}^{R,TF}$) for $i = 1, 2, 3$. In the fractional models, α^{opt} is set as 0.76, 0.58 and 0.51 for $\mathcal{L}_\delta = 4, 8, 12$, respectively.

specified interval for $\mathcal{L}_\delta = \mathcal{L}/2\delta x = 4, 8, 12$, respectively, where $\delta x = 2\pi/N$ represents the computational grid size.

From the kinetic perspective, enlarging $\mathcal{L}_\delta$, $\overline{f^{eq}(\Delta)}$ in (3.6) demonstrates an increasingly multi-exponential pattern, which can be better described by a power-law distribution function. This argument accounts for the prediction enhancement in figure 1, achieved by the TFSGS model and the abduct reduction of α^{opt} vs $\mathcal{L}_\delta$ (see Samiee *et al.* 2020*a*, p. 10). Theoretically, the tempered power-law distribution can resemble a power-law or a Gaussian distribution by letting λ go to 0 or ∞, respectively. This allows the TFSGS model to span the gap between the FSGS model, representing self-similar behaviour of the inertial range, and the SMG model, renowned for its dissipative characteristics. The results in table 2 support this line of reasoning by a row of correlation quantities for the given filter widths, particularly at $\mathcal{L}_\delta = 12$.

On this background, we proceed with the second step in algorithm 1 to indicate λ^{opt} through a comparative study of the normalized stress–strain correlation function, defined as $S_\Delta = D_{LL}(r, t)/D_{LL}(0, t)$. With the knowledge of $D_{LL}(r, t)$, we extend the two-point correlation analysis to the spectral space by evaluating the instantaneous radial dissipation spectrum, given by $\hat{\mathcal{D}}(\xi) = \mathcal{F}[D_{LL}(r, t)](\xi)$. To evaluate the error between the dissipation spectrum, obtained by the true DNS data and the LES models at high wave numbers, we define

$$\mathcal{E}_H = \frac{\left| \left[\hat{\mathcal{D}}(\xi)\right]^* - \left[\hat{\mathcal{D}}(\xi)\right]^D \right|}{\left| \left[\hat{\mathcal{D}}(\xi)\right]^D \right|}, \tag{5.1}$$

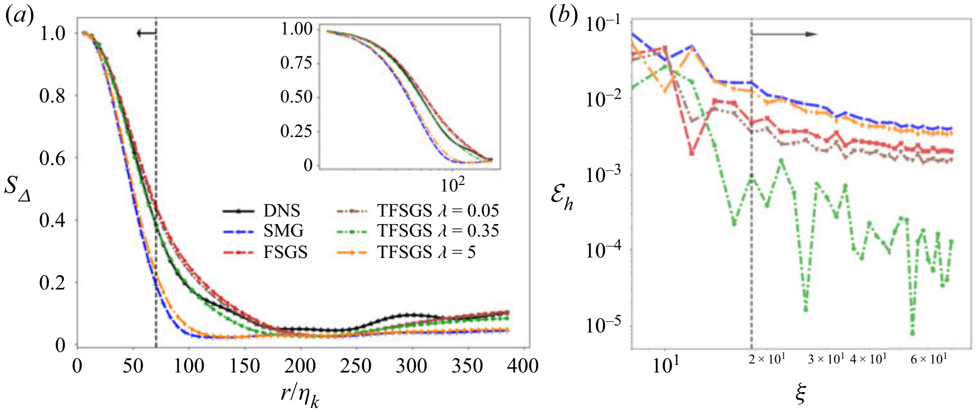

Figure 2. (*a*) Comparing results of the normalized two-point stress–strain rate correlation functions (S_Δ) and (*b*) error analysis of the longitudinal dissipation spectrum ($\mathcal{E}_H$) for FSGS and SMG models, where $\mathcal{L}_\delta = 8$ and ξ represents the radius of Fourier wave numbers. In both plots, the arrows point to the dissipation range.

where $|\cdot|$ represents the norm of the vector. Figure 2(*a*) displays S_Δ vs the spatial shift, r, for a logarithmic sequence of λ spanning three orders of magnitude in the TFSGS model, where $\mathcal{L}_\delta = 8$. As stated earlier, the proposed model can take a journey from the FSGS to the SMG models by tuning λ. Evidently, the true quantities of S_Δ, coloured black, are well predicted by the proposed model with $\lambda^{opt} = 0.45$, where $\alpha^{opt} = 0.58$ is fixed. Figure 2(*b*) confirms our findings quantitatively in a plot of $\mathcal{E}_H$ vs radius of wave numbers, ξ, with log-scale axes. In fact, this plot implies accuracy of the TFSGS model in capturing the two-point structure function at the dissipation range, as pointed by an arrow.

Employing the same analysis for $\mathcal{L}_\delta = 4,\ 12$, we infer the optimal behaviour of the TFSGS model, evaluated for a logarithmic range of λ with a fixed α^{opt}, in figure 3. The inset plots show $\mathcal{E}_H$ vs ξ using log-scale on both axes to magnify the dissipation range at high wave numbers. Interestingly, at $\mathcal{L}_\delta = 4$ the FSGS model is dissipative enough to outperform the tempered model in capturing the true S_Δ in figure 3(*a*). With all this in mind, these results certify the importance of tempering in correct regeneration of two-point correlation functions particularly at larger filter widths ($\mathcal{L}_\delta = 8,\ 12$). Moreover, the SMG model, resembling the TFSGS with $\lambda \sim 5$, exhibits a relatively steeper slope at the dissipation range, which is rooted in the diffusive form of its operator. In this context, tempering plays a crucial role in characterizing dissipation structures covering the widening gaps between the asymptotic cases ($\lambda = 0.01$ and 5) in figure 3(*b*). This brings up the TFSGS model as a superior physics-based model in comparison with its counterparts, i.e. the SMG and FSGS models.

Given the values of α^{opt} and λ^{opt}, we proceed lastly with quantifying $c_{\alpha,\lambda}$ as prescribed in algorithm 1. Under statistically stationary circumstances of the flow field, $c_{\alpha,\lambda}$ remains fairly unchanged for each $\mathcal{L}_\delta$ of interest, as reported in table 3. It should be noted that $c_{\alpha,\lambda}$ is part of the fractional coefficient, described in (4.4), to scale up the model in a constant Re_λ and $\mathcal{L}_\delta$.

5.3. *Interpretation of two-point structure functions*

The third-order structure functions, arising from the KH equations, provide insights about the statistics of unresolved scales and their strong interactions with large-scale motions. As discussed previously in § 4, $G_\Delta = G_{LLL}/\epsilon\mathcal{L}$, representing the scaled two-point

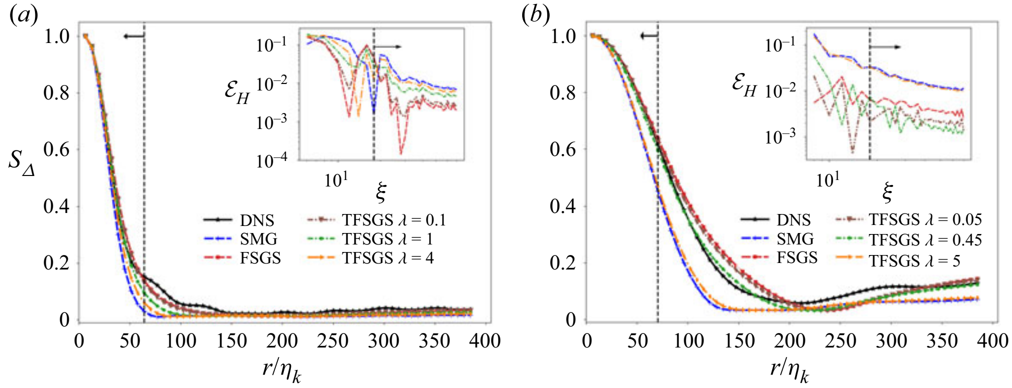

Figure 3. Comparing results of the normalized two-point stress–strain rate correlation functions for (a) $\mathcal{L}_\delta = 4$ and (b) $\mathcal{L}_\delta = 12$. The inset plots illustrate the normalized error of longitudinal dissipation spectrum ($\mathcal{E}_H$) vs the radius of Fourier wave numbers (ξ). The arrows point to the dissipation range.

$\mathcal{L}_\delta = 4$			$\mathcal{L}_\delta = 8$			$\mathcal{L}_\delta = 12$		
α	λ	$c_{\alpha,\lambda}$	α	λ	$c_{\alpha,\lambda}$	α	λ	$c_{\alpha,\lambda}$
0.76	$\simeq 0$	2.08	0.58	0.35	0.88	0.51	0.45	0.048

Table 3. Optimized parameters associated with the TFSGS model in terms of algorithm 1 for differing filter widths.

velocity-stress correlation function, is introduced as a sufficient condition for precise regeneration of third-order structure functions and an *a priori* consistency in LES modelling. Following the derivation of the longitudinal Taylor macroscale in Pope (2000, chap. 6), $D_{LL}(r)$ seems to be directly connected to the first-order derivative of $G_{LLL}(r)$ at the dissipation range. This offers the capability of the optimum edition of the TFSGS model in capturing G_Δ and thereby fulfilling the essential conditions in (4.2).

In the first stage of the statistical analysis, we perform a comprehensive study on G_Δ in figure 4(a) for $\mathcal{L}_\delta = 8$, in which the dissipation and inertial ranges are magnified in figure 4(b) with a semi-logarithmic scale on the x-axis and figure 4(c) with logarithmic scales on both axes, respectively. The balance regions (BR), including extremum points, are thickened up in all the graphs in figure 4(a). Balance regions also indicate the transitional zone between dissipation and inertial ranges. Aligned with the right side of (4.2), the trend of G_Δ at small-scale interactions appear to be a linear function of spatial displacement, r, suggested by Meneveau (1994, figure 2). The results in figure 4(a) and more accurately in figure 4(b) offer that the optimum TFSGS model well predicts the true DNS quantities at the left side of the BR, not only the slope of G_Δ but also the maximum of G_Δ occurring at a relatively close r. This spotlights the importance of step three of algorithm 1 in tuning the slope of G_Δ at the dissipation range and the effective role of the tempering parameter in fitting the BR, associated with the filtered DNS data. In practice, increasing λ pushes the BR toward the left side to preserve the increasing linear correlation as a notion of more dissipative behaviour. These findings are endorsed qualitatively for the other filter widths in figure 5, considering λ^{opt} in table 3.

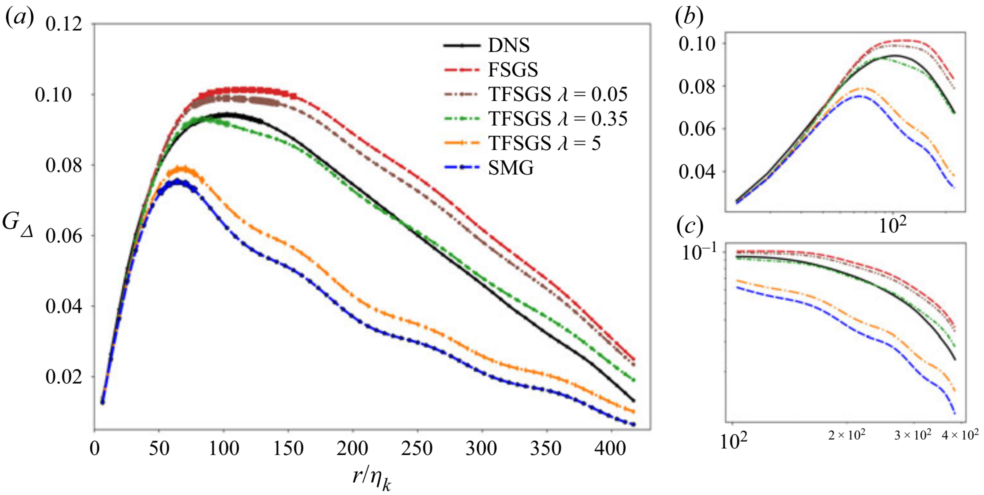

Figure 4. Two-point velocity-stress correlation function in a stationary HIT flow for $\mathcal{L}_\delta = 8$ using box filtering. The segment of the balance region (BR) has been thickened up in (*a*) for all the graphs. The dissipation and the inertial ranges have been enlarged in plots (*b*) with semi-logarithmic scale on the *x*-axis and (*c*) with a logarithmic scale on both axes, respectively.

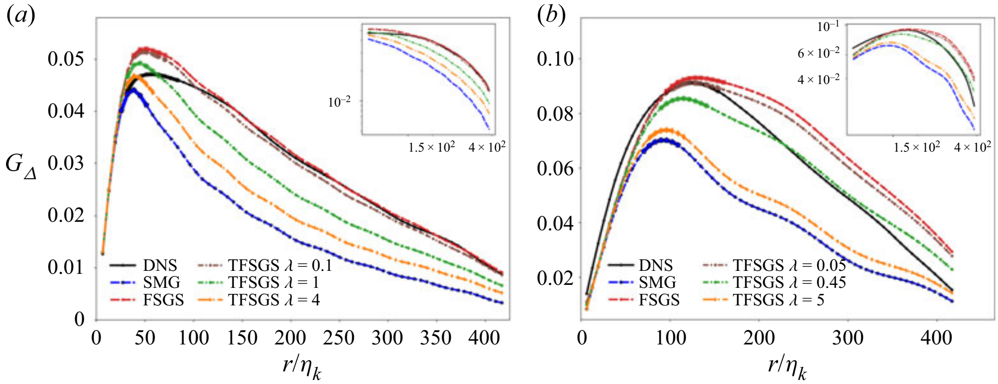

Figure 5. Two-point velocity-stress correlation function in a stationary HIT flow for (*a*) $\mathcal{L}_\delta = 4$ and (*b*) $\mathcal{L}_\delta = 12$ using box filtering. The inertial range has been enlarged in the inset plots with a logarithmic scale on both axes.

In analysis of G_Δ at the inertial range, the graph, associated with λ^{opt}, shows a favourable match with true points, coloured black, in figures 4 and 5. For the purpose of clarity, the inertial ranges are magnified in log-log scale plots in figure 4(*c*) for $\mathcal{L}_\delta = 8$ and the inset plots in figure 5 for $\mathcal{L}_\delta = 4,\ 12$, respectively. Motivated by these results, tempered fractional modelling seems to be faithful in fitting structures at the dissipation and the inertial ranges and also estimating the correct value of *r*, associated with the extremum points. Inevitably, enlarging $\mathcal{L}_\delta$ accounts for inaccuracies in fitting the tail of graphs as observed in 5(*b*). Notwithstanding, the mid-range interactions are acceptably predicted by the optimized TFSGS model.

With an overview of the present results, the TFSGS model stands out as a structure-based approach, which reasonably covers the gap between the FSGS and SMG models. In $\mathcal{L}_\delta = 4$, λ^{opt} is found to be very close to zero, which renders tempering

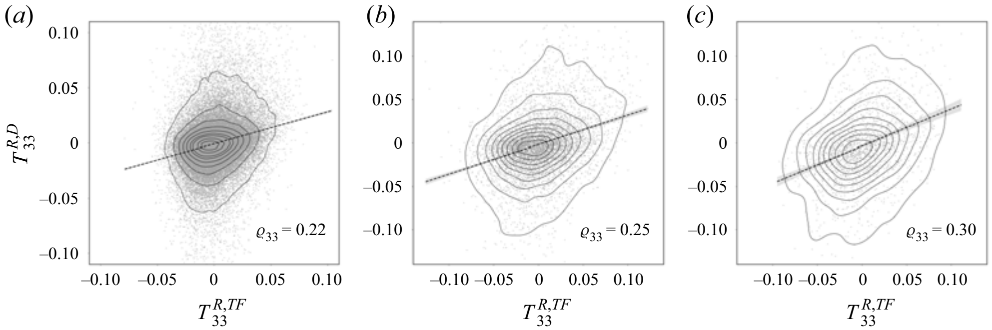

Figure 6. Scatter plots of the SGS stresses obtained by the filtered DNS data ($\boldsymbol{T}_{33}^{R,D}$) vs the modelled stresses ($\boldsymbol{T}_{33}^{R,TF}$) using optimized parameters in table 3 for (*a*) $\mathcal{L}_\delta = 4$, (*b*) $\mathcal{L}_\delta = 8$ and (*c*) $\mathcal{L}_\delta = 12$.

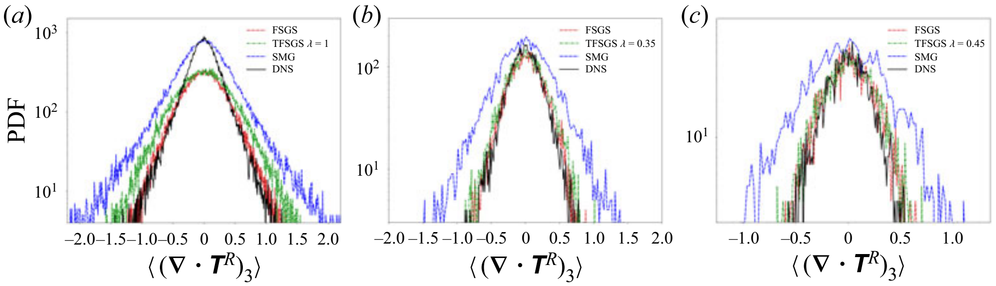

Figure 7. Probability density function of the ensemble-averaged $(\nabla \cdot \boldsymbol{T})_{i=3}$ for the optimized (tempered) fractional and the SMG models at (*a*) $\mathcal{L}_\delta = 4$, (*b*) $\mathcal{L}_\delta = 8$ and (*c*) $\mathcal{L}_\delta = 12$.

non-essential in capturing two-point structures. As we increase $\mathcal{L}_\delta$, this gap starts widening up and the tempering mechanism acts more dynamically in finding the true BR and fitting the dissipation structures. This argument confirms that the tempered fractional approach displays great potential for parameterizing structure function especially at larger filter widths while retaining fairly acceptable accuracy.

5.4. *Probability density function of SGS stresses*

Within the proposed statistical framework, the last step in algorithm 1 focuses on the probability density functions (PDFs) of filtered DNS data. The key idea is to assess the performance of models and verify if the proposed model maintains the true statistics. In this context, we present the scatter plots of $\boldsymbol{T}_{ii}^{R,D}$ against $\boldsymbol{T}_{ii}^{R,TF}$ in figure 6 for three given filter widths and $i = 3$. We should note that the present results are confined to $i = 3$ due to the similarities in other directions. The slope in each plot is indicated by the corresponding correlation coefficients in table 2. The most noticeable specific about these results is that the data points are bounded within a same order of magnitude on both axes. As a matter of fact, we achieve a roughly unit regression coefficient between $\boldsymbol{T}_{ii}^{R,D}$ and $\boldsymbol{T}_{ii}^{R,TF}$, where our optimization strategy targets for correct estimation of the SGS dissipation. This analysis can be extended to the PDF plots in figure 7. With nearly the same correlation coefficients, the SMG model fails to reproduce the true statistics, while the optimum TFSGS model offers a great match with the true graphs. As pointed out previously, in $\mathcal{L}_\delta = 4$ the FSGS model represents the equivalent form of the TFSGS with $\alpha^{opt} = 0.76$ and $\lambda^{opt} \simeq 0$.

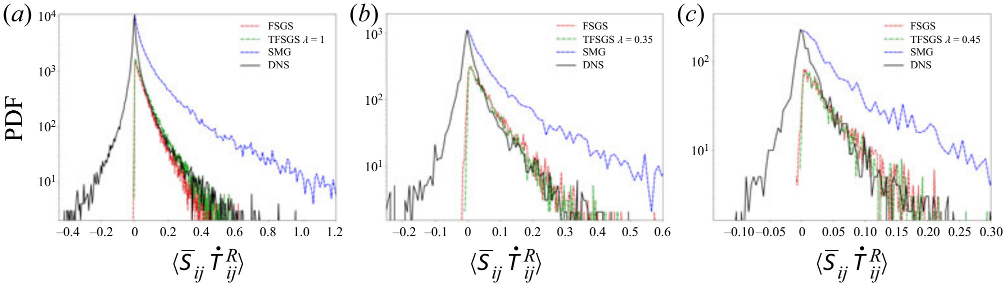

Figure 8. Probability density function of the ensemble-averaged SGS dissipation for the optimized (tempered) fractional and the SMG models at (*a*) $\mathcal{L}_\delta = 4$, (*b*) $\mathcal{L}_\delta = 8$ and (*c*) $\mathcal{L}_\delta = 12$.

From the understanding of energy cascading in turbulent flows, the SGS dissipation, ϵ, is considered as an external parameter in two-point structure equations for describing small-scale motions. In the statistical sense, we compare the PDFs of ϵ, implied by the models, with the true PDFs, obtained by the filtered DNS data for $\mathcal{L}_\delta = 4, 8, 12$. As shown in figure 8, the fractional models accurately predict the forward scattering, associated with the positive dissipation, ϵ^+, while the SMG model appears to be too dissipative due to its positive eddy viscosity. Furthermore, the TFSGS model presents an underprediction of the backward scattering by producing a slim amount of negative dissipation, ϵ^-. On the side of numerical analysis, this limitation results in preserving numerical stability by minimizing negative dissipation error.

5.5. *A posteriori analysis*

With a focus on numerical stability, we extend the statistical *a priori* assessments to an *a posteriori* analysis in order to evaluate performance of the proposed models in time. We employ the pseudo-spectral solver, described in § 5.1, on $\varOmega$ discretized with a uniform grid of 520^3 resolution, and resolve over 5 eddy turnover times, $\tau_{\mathscr{L}}$, to provide the DNS flow fields. The simulation is initiated with an instantaneous flow field, obtained from the sufficiently resolved DNS of a stationary HIT flow at $Re_\lambda = 240$. The comprehensive characteristics of this fully developed turbulent field are reported in Akhavan-Safaei & Zayernouri (2020). By the explicit filtering of this initial flow field, the *a posteriori* simulations are carried out on 130^3 and 52^3 grids for the corresponding $\mathcal{L}_\delta = 2, 5$, respectively.

This analysis allows for structural comparisons between the fractional models and the filtered DNS data through tracking the evolution of resolved turbulent kinetic energy, $K_{tot}(t) = \langle \bar{V}_i \bar{V}_i / 2 \rangle_s$. Figure 9 displays the decay of the resolved kinetic energy, which verifies computational stability of the fractional models. The TFSGS models associated with $\alpha = 0.7$ and $\lambda = 0.3$ for $\mathcal{L}_\delta = 2$, and $\alpha = 0.6$ and $\lambda = 0.5$ for $\mathcal{L}_\delta = 5$ present a favourable match with the true decaying of K_{tot} compared with the SMG and dynamic SMG models. These results spotlight the importance of tempering in the correct prediction of kinetic energy while by increasing λ, the TFSGS model asymptotes overpredictions of the SMG model for both $\mathcal{L}_\delta = 2, 5$.

Given the *a priori* analysis in previous subsections, the model parameters are fitted through satisfying both sides of (4.2), which are inherently connected with the second- and third-order structure functions. In figure 10 we study the two-point second-order structure functions, B_{LL}, after 2 and 4 eddy turnover times of simulation. It should be noted that

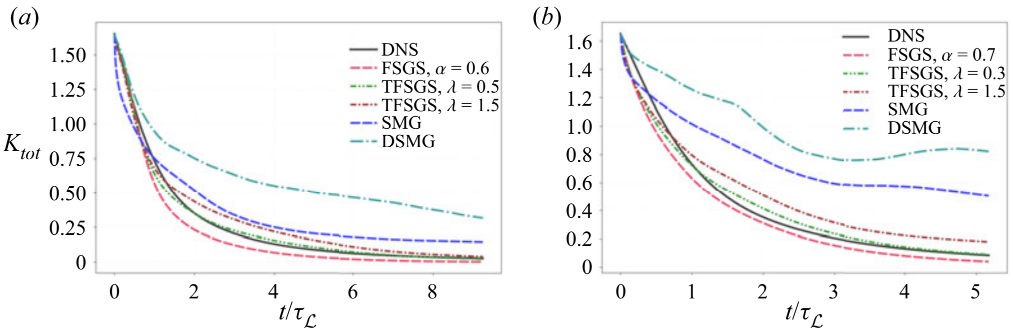

Figure 9. Decay of the resolved turbulent kinetic energy, K_{tot}, for the optimized TFSGS and the SMG models with (*a*) 52^3 and (*b*) 130^3 grid points.

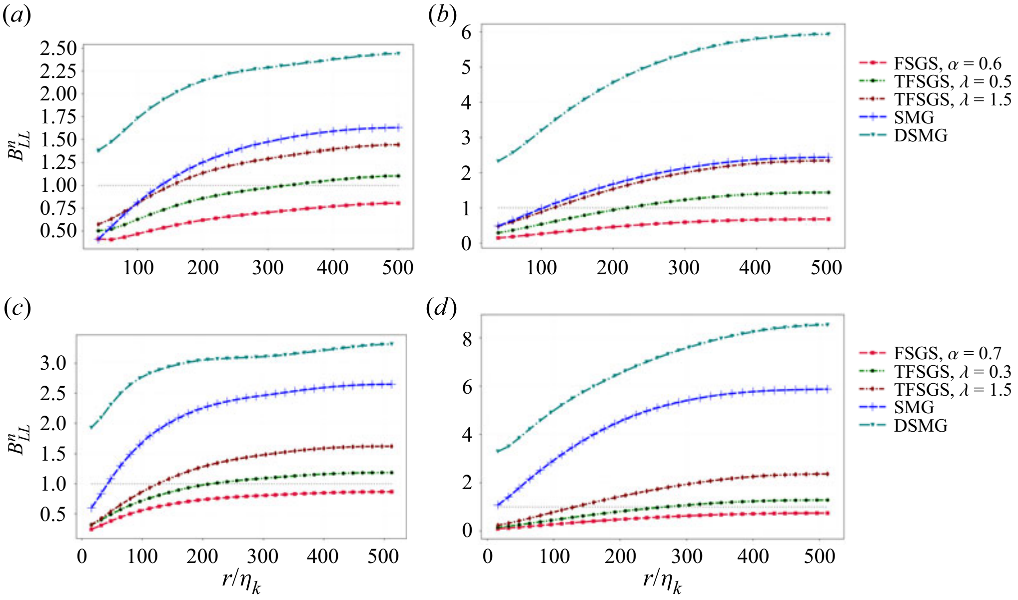

Figure 10. Two-point second-order structure functions of the resolved velocity fields normalized by the filtered DNS data for (*a*,*b*) $\mathcal{L}_\delta = 5$ and (*c*,*d*) $\mathcal{L}_\delta = 2$ at $t = 2\tau_{\mathscr{L}}$ and $t = 4\tau_{\mathscr{L}}$, respectively.

B^n_{LL} and B^n_{LLL} represent the second- and third-order correlation functions from the LES models, which are normalized by the corresponding filtered DNS solutions, respectively. Supported by the results in figure 10, the TFSGS model, associated with the optimum λ, maintains B_{LL} over a wide range of r although presenting small inconsistencies at small scales. As an essential condition to a physically accurate SGS model, the optimized TFSGS also provides a fairly accurate and reliable prediction of B_{LLL} compared with the FSGS and the eddy-viscosity approaches in figure 11. In this vein, we also present the energy spectra, E_ξ, resulting from the LES for different values of λ in figure 12 and compare it with the corresponding E_ξ from the DNS results at $t = 2\tau_{\mathcal{L}}$ and $4\tau_{\mathcal{L}}$.

In most of the LES approaches, fidelity in representing spatial structures is essentially compromised in order to preserve the numerical stability by inducing the excessive amount of energy dissipation. Nevertheless, the present results verify our findings in § 4 that the TFSGS model provides stable LES solutions while preserving high-order structure functions in *a priori* and also *a posteriori* tests.

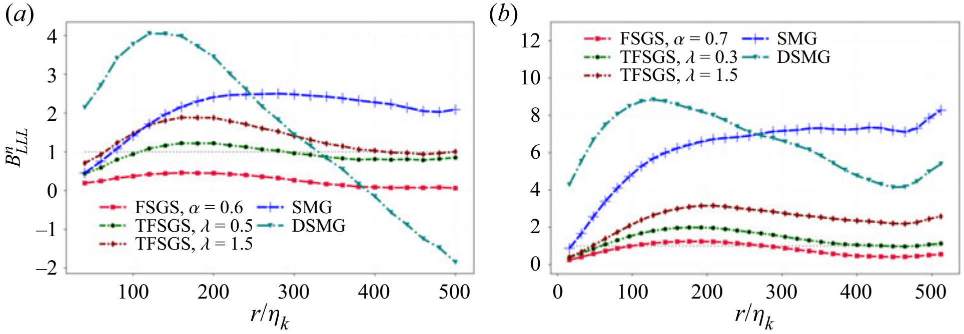

Figure 11. Third-order structure functions of the resolved velocity fields normalized by the filtered DNS data for (*a*) $\mathcal{L}_\delta = 5$ and (*b*) $\mathcal{L}_\delta = 2$ at $t = 4\tau_{\mathscr{L}}$.

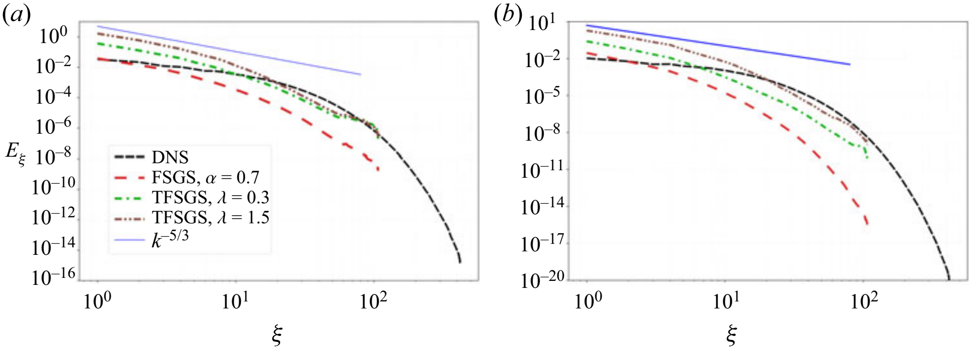

Figure 12. Energy spectra (E_ξ) vs ξ, resulting from 130^3 LES cases with the TFSGS models evaluated for $\alpha = 0.7$ and $\lambda = 0, 0.3, 1.5$ for $\mathcal{L}_\delta = 2$ at (*a*) $t = 2\tau_{\mathscr{L}}$ and (*b*) $t = 4\tau_{\mathscr{L}}$.

5.6. *Merits, challenges and future works*

On the basis of *a priori* and *a posteriori* analyses, the present work provides a robust physics-based framework for fractional LES modelling of SGS structures. The significance of this approach lies in the following.

(i) We treat the source of turbulent small-scale motions at the kinetic level, by employing a tempered heavy-tailed distribution in approximating $\overline{f^{eq}}$. This leads us to the tempered fractional operator in the filtered NS equations as a proper choice for modelling a power-law like behaviour in the mid-range and a Gaussian tail in real-physics anomalous phenomena.

(ii) The proposed TFSGS model sets the ground for fulfilling essential statistical conditions as a relatively best approximation of an ideal LES model through fractional and tempering parameters. To achieve an optimized edition of the TFSGS model, we devise an optimization strategy, which involves conventional one-point correlation coefficients, two-point structures and the SGS dissipation.

(iii) The optimized TFSGS model presents reasonably accurate predictions of two-point structure functions for a range of filter widths while maintaining the expected correlations between the modelled and true SGS stresses.

(iv) The corresponding fractional LES solutions present a stable prediction of turbulent kinetic energy while preserving high-order structure functions in the *a posteriori* analysis.

Despite the theoretical and statistical challenges and achievements, we believe this approach shows a viable and promising direction toward non-local modellings of turbulence. By employing more sophisticated and physically consistent distributions in approximating $\overline{f^{eq}(\Delta)}$ (e.g. distributed-order tempered power laws), we can even attain better accuracy and enhanced performance. On the theoretical side, the current framework deserves a careful mathematical attention to be extended to anisotropic, yet homogeneous, flows employing proper forms of distributions at the kinetic level. Moreover, further works should be undertaken to generalize the fractional model to a data-driven representation of spatial and temporal structures in more complex turbulent regimes.

6. Conclusions and remarks

Inspired by non-locality, embedded in interactions between large- and small-scale motions, we developed a TFSGS model for LES of HIT flows. We began with modelling of turbulent effects at the kinetic level by closing the collision term in the filtered BT equation. To approximate multi-exponential behaviours of the filtered equilibrium distribution in the collision operator, we employed a tempered Lévy-stable distribution function, which presents a power law at a moderate range and then converges to an exponential decay. By ensemble averaging of the approximated BT, we derived the LES equations, in which the divergence of SGS stresses emerged as a summation of tempered fractional Laplacian, $(\Delta + \lambda)^{\alpha}(\cdot)$, where $\alpha \in (0, 1)$, $\alpha \neq \frac{1}{2}$ and $\lambda > 0$. Interestingly, the FSGS is found to be a particular form of the TFSGS model when λ approaches 0. Moreover, we formulated the SGS stresses straightforwardly in terms of a combination of integer and fractional operators, which gives the advantage of being feasible and quite easy to implement in the Fourier space. The corollary on the frame invariant property of the FSGS model was also extended to the current model, showing its physical and mathematical consistency.

In a statistical framework, we constructed a structure based algorithm for optimizing the fractional models, which involved the closed essential conditions for a weaker sense of an ideal LES model. Following the optimization strategy, we inferred the optimum tempering parameter through a comparative study of two-point stress–strain correlation functions while the fractional exponent was fixed for maintaining reasonable values of correlation coefficients. Next, we quantified the fractional coefficient using SGS dissipation as a crucial factor in identifying high-order structures. The more profound analysis of dissipation structure functions emphasized on the central role of λ in spanning the gap between the FSGS and SMG models, especially at larger $\mathcal{L}_{\delta}$, when α^{opt} decreases. Regarding the KH equation, the optimum TFSGS model presented a great match with the true values of two-point velocity-stress correlation functions, which ensures the accurate prediction of third-order structure functions.

The success of the tempering mechanism in capturing structure correlation functions, particularly at larger $\mathcal{L}_{\delta}$, originated from the capabilities of our choice in fitting semi-heavy-tailed behaviour of the filtered equilibrium distribution at the kinetic level. The inspection of statistical results also supported accuracy of the fractional model in keeping unit regression and capturing the corresponding PDF tails. As a notion of numerical stability, we demonstrated that the optimized TFSGS model well predicted the true forward scattering in a statistical sense without generating any significant negative dissipation.

Lastly, the TFSGS model underwent the ultimate *a posteriori* analysis, which verified a numerically stable performance of the fractional model through tracking the resolved turbulent kinetic energy. With the emphasis on remarkable potentials and merits of the present work, we believe that this approach can be extended to more complex turbulent flows by employing a variety of rigorous fractional operators, derived from the statistical structures.

Acknowledgements. The high-performance computing resources and services were provided by the Institute for Cyber-Enabled Research (ICER) at Michigan State University.

Funding. This work was financially supported by the MURI/ARO grant (W911NF-15-1-0562), the ARO Young Investigator Program (YIP) award (W911NF-19-1-0444), and partially by the National Science Foundation award (DMS-1923201).

Declaration of interests. The authors report no conflict of interest.

Author contributions. Mehdi Samiee served as a PhD student on this project, and was in charge of deriving the model, developing the code based on an earlier PoF work, partially in charge of running the simulations, in addition to the statistical analyses and visualizing the data, and preparing the manuscript.

Ali Akhavan-Safaei served as a PhD student on this project, and was partially in charge of running the simulations, developing the code and analysing the data, in addition to assisting with the preparation of the manuscript.

Mohsen Zayernouri served as the PI and PhD advisor on the project, being in charge of the funding support, conceptualizing of the project and planning, providing advice on the simulations and statistical analyses, assisting with the writing original/revised manuscript, and serving as the corresponding author.

Author ORCIDs.
Ali Akhavan-Safaei https://orcid.org/0000-0002-0812-1881;
Mohsen Zayernouri https://orcid.org/0000-0002-0831-2610.

Appendix A

As noted in Deng *et al.* (2018), Di Nezza, Palatucci & Valdinoci (2012), the tempered fractional Laplacian operator can be represented in various equivalent forms, i.e.

$$\begin{aligned}(\varDelta+\lambda)^{\alpha}u(\boldsymbol{x}) &= -C_{d,\alpha}\,\mathrm{P.V.}\int_{\mathbb{R}^d}\frac{u(\boldsymbol{x})-u(\boldsymbol{\mathfrak{s}})}{\mathrm{e}^{\lambda|\boldsymbol{x}-\boldsymbol{\mathfrak{s}}|}\,|\boldsymbol{x}-\boldsymbol{\mathfrak{s}}|^{2\alpha+d}}\,\mathrm{d}\boldsymbol{\mathfrak{s}}\\ &= \frac{C_{d,\alpha}}{2}\,\mathrm{P.V.}\int_{\mathbb{R}^d}\frac{u(\boldsymbol{x}+\boldsymbol{\mathfrak{s}})+u(\boldsymbol{x}-\boldsymbol{\mathfrak{s}})-2u(\boldsymbol{x})}{\mathrm{e}^{\lambda\mathfrak{s}}\,\mathfrak{s}^{2\alpha+d}}\,\mathrm{d}\boldsymbol{\mathfrak{s}},\end{aligned}\tag{A1}$$

where $\mathfrak{s}=|\boldsymbol{\mathfrak{s}}|$, $\alpha\in(0,\frac{1}{2})\cup(\frac{1}{2},1)$, and $\lambda>0$. By performing the Fourier transform of (A1), we get

$$\begin{aligned}\mathcal{F}\left[(\varDelta+\lambda)^{\alpha}u(\boldsymbol{x})\right](\boldsymbol{\xi}) &= \frac{C_{d,\alpha}}{2}\int_{\mathbb{R}^d}\frac{\mathrm{e}^{\boldsymbol{\xi}\cdot\boldsymbol{\mathfrak{s}}}+\mathrm{e}^{-\boldsymbol{\xi}\cdot\boldsymbol{\mathfrak{s}}}-2}{\mathrm{e}^{\lambda\mathfrak{s}}\,s^{2\alpha+d}}\,\mathrm{d}\boldsymbol{\mathfrak{s}}\\ &= -C_{d,\alpha}\int_{\mathbb{R}^d}\frac{1-\cos(\boldsymbol{\xi}\cdot\boldsymbol{\mathfrak{s}})}{\mathrm{e}^{\lambda\mathfrak{s}}\,\mathfrak{s}^{n+2\alpha}}\,\mathrm{d}\boldsymbol{\mathfrak{s}}\,\mathcal{F}\left[u(\boldsymbol{x})\right](\boldsymbol{\xi}),\end{aligned}\tag{A2}$$

in which $\boldsymbol{\xi}$ denotes the Fourier numbers. For the sake of simplicity, we define

$$I(\boldsymbol{\xi}) = -\int_{\mathbb{R}^d}\frac{1-\cos(\boldsymbol{\xi}\cdot\boldsymbol{\mathfrak{s}})}{\mathrm{e}^{\lambda\mathfrak{s}}\,\mathfrak{s}^{n+2\alpha}}\,\mathrm{d}\boldsymbol{\mathfrak{s}},\tag{A3}$$

which appears to be rotationally invariant. Moreover, we introduce $\xi=|\boldsymbol{\xi}|$ and $\mathfrak{s}_{\theta}=\mathfrak{s}\cos(\theta)$. Without loss of generality, θ can be chosen such that $\mathfrak{s}\cos(\theta)$ is aligned with the first primary direction. Therefore, $I(\boldsymbol{\xi})$ can be re-expressed by

$$I(\boldsymbol{\xi}) = \int_{\mathbb{R}^d} \frac{\cos(\boldsymbol{\xi}\cdot\boldsymbol{\mathfrak{s}}) - 1}{\mathrm{e}^{\lambda \mathfrak{s}}\, \mathfrak{s}^{n+2\alpha}}\, \mathrm{d}\boldsymbol{\mathfrak{s}} = \int_{\mathbb{R}^d} \frac{\cos(\eta_\theta) - 1}{\mathrm{e}^{\lambda\eta/\xi}\,(\eta/\xi)^{n+2\alpha}} \frac{\mathrm{d}\boldsymbol{\eta}}{\xi^n} = \xi^{2\alpha} \int_{\mathbb{R}^d} \frac{\cos(\eta_\theta) - 1}{\mathrm{e}^{\lambda\eta/\xi}\,(\eta)^{n+2\alpha}}\, \mathrm{d}\boldsymbol{\eta}, \tag{A4}$$

where $\boldsymbol{\eta} = \xi\boldsymbol{\mathfrak{s}}$, $\eta = |\boldsymbol{\eta}|$ and $\eta_\theta = \xi\mathfrak{s}_\theta$. Due to the invariant properties of $I(\boldsymbol{\xi})$, we proceed the derivations with transforming (A4) into the corresponding spherical coordinate, $(\mathrm{r}, \phi_1, \ldots, \phi_{d-1})$.

In terms of the transformation, we let $\eta = |\boldsymbol{\eta}| = r$ and $\eta_\theta = \eta\cos(\theta) = r\cos(\phi_1)$. Then, in a general case for $d > 1$, $\mathrm{d}\boldsymbol{\eta}$ follows

$$\mathrm{d}\boldsymbol{\eta} = \mathcal{J}(r, \phi_1, \ldots, \phi_{d-1})\, \mathrm{d}r\, \mathrm{d}\phi_1 \ldots \mathrm{d}\phi_{d-1}, \tag{A5}$$

where

$$\mathcal{J}(r, \phi_1, \ldots, \phi_{d-1}) = \left|\det \frac{\partial x_i}{\partial (r\phi_j)}\right| = r^{d-1} \sin^{d-2}(\phi_1) \sin^{d-3}(\phi_2) \ldots \sin(\phi_{d-2}) \tag{A6}$$

for $i = 1, \ldots, d$ and $j = 1, \ldots, d-1$ (see Henderson & Taimina 2000). Therefore, we find the general form of $I(\boldsymbol{\xi})$ as

$$I(\boldsymbol{\xi}) = \xi^{2\alpha}\, \bar{c} \int_0^\infty \int_0^{2\pi} \frac{\cos\left(r\cos(\phi_1)\right) - 1}{\mathrm{e}^{\lambda r/\xi}\,(r)^{d+2\alpha}}\, r^{d-1} \sin^{d-2}(\phi_1)\, \mathrm{d}\phi_1\, \mathrm{d}r, \tag{A7}$$

where $\bar{c} = \int_0^\pi \sin^{d-3}(\phi_2)\, \mathrm{d}\phi_2 \ldots \int_0^\pi \sin(\phi_{d-1})\, \mathrm{d}\phi_{d-1} = 2\pi^{(d-1)/2}/\Gamma((d-1)/2)$. It is shown by Deng *et al.* (2018) that

$$\begin{aligned} I(\boldsymbol{\xi}) &= \bar{c}\,\xi^{2\alpha} \int_0^\infty \frac{\mathrm{e}^{-\lambda r/\xi}}{r^{\beta+1}} \int_0^{2\pi} \left[\cos\left(r\cos(\phi_1)\right) - 1\right] \sin^{d-2}(\phi_1)\, \mathrm{d}\phi_1\, \mathrm{d}r \\ &= \frac{\bar{c}\,\Gamma(-2\alpha)\pi^{1/2}\Gamma\left(\dfrac{d-1}{2}\right)}{\Gamma\left(\dfrac{d}{2}\right)} \left[\lambda^2 - (\lambda^2 + \xi^2)^\alpha\, {}_2F_1\left(-\alpha, \frac{d+2\alpha-1}{2}; \frac{d}{2}; \frac{\xi^2}{\xi^2 + \lambda^2}\right)\right], \end{aligned} \tag{A8}$$

where ${}_2F_1$ denotes a Gaussian hypergeometic function. Therefore,

$$\mathcal{F}\left[(\Delta + \lambda)^\alpha u(\boldsymbol{x})\right](\boldsymbol{\xi}) = \mathfrak{C}_{d,\alpha} \times \left[\lambda^2 - (\lambda^2 + \xi^2)^\alpha\, {}_2F_1\left(-\alpha, \frac{d+2\alpha-1}{2}; \frac{d}{2}; \frac{\xi^2}{\xi^2 + \lambda^2}\right)\right], \tag{A9}$$

where $\mathfrak{C}_{d,\alpha} = C_{d,\alpha}\,\bar{c}\,\Gamma(-2\alpha)(\pi^{1/2}\Gamma((d-1)/2)/\Gamma(d/2)) = 1/{}_2F_1(-\alpha, (d+2\alpha-1)/2; d/2; 1)$.

Appendix B

As we discussed in subsection 3.3, the SGS stresses are described by

$$\boldsymbol{T}^R_{ij} = \frac{\rho\, c_{\beta,\lambda}}{U^3} \int_0^\infty \int_{\mathbb{R}^3} (u_i - \bar{V}_i)(u_j - \bar{V}_j) \left(F^{\beta,\lambda}(\bar{\Delta}_s) - F^{\beta,\lambda}(\bar{\Delta})\right) \mathrm{e}^{-s}\, \mathrm{d}\boldsymbol{u}\, \mathrm{d}s, \tag{B1}$$

where $F^{\beta,\lambda}(\bar{\Delta})$ represents a tempered Lévy β-stable distribution. Let us consider $\beta = -\alpha - \frac{3}{2}$ for $\alpha \in (0, \frac{1}{2}) \cup (\frac{1}{2}, 1)$. Regarding the equivalent Pareto-like behaviour of Lévy distributions (Weron 2001) at $\bar{\varDelta} > 1$, we decompose the domain of kinetic momentum such that $\mathbb{R}^3 = \mathcal{I}_\epsilon \cup (\mathbb{R}^3 \setminus \mathcal{I}_\epsilon)$, where $\mathcal{I}_\epsilon = \{u \in \mathbb{R}^d \ s.t. \ |\bar{\varDelta}| < \epsilon\}$ and $\epsilon \ll 1$. This allows for the approximation

$$F^{\alpha,\lambda}(\bar{\varDelta}) \simeq C_\alpha \begin{cases} 0, & \boldsymbol{u} \in \mathcal{I}_\epsilon, \\ \mathrm{e}^{-\lambda\,\bar{\varDelta}^{1/2}}\,\bar{\varDelta}^{-(\alpha+3/2)}, & \boldsymbol{u} \in \mathbb{R}^3 \setminus \mathcal{I}_\epsilon, \end{cases} \tag{B2}$$

where $C_\alpha = (-\varGamma(3/2)/2\pi^{3/2}\varGamma(-2\alpha))(1/{}^2F_1(-\alpha, 1+\alpha; 3/2; 1))$. It is worth mentioning that $F^{\alpha,\lambda}(\bar{\varDelta})$ reduces exponentially in a close proximity of $\bar{\varDelta} = 0$. With all this in mind, the approximated function of $F^{\alpha,\lambda}(\bar{\varDelta})$ in (B2) can properly capture the heavy-tailed behaviour of the filtered collision term. Evidently, by replacing $\mathrm{e}^{-\lambda\bar{\varDelta}_s^{1/2}}$ with $\mathrm{e}^{-\lambda\bar{\varDelta}^{1/2}}$ for $\bar{\varDelta} > 1$, we arrive at the expression

$$\begin{aligned} F^{\alpha,\lambda}(\bar{\varDelta}_s) - F^{\alpha,\lambda}(\bar{\varDelta}) &= C_\alpha \left(\frac{\mathrm{e}^{-\lambda\bar{\varDelta}_s^{1/2}}}{\bar{\varDelta}_s^{(\alpha+3/2)}} - \frac{\mathrm{e}^{-\lambda\bar{\varDelta}^{1/2}}}{\bar{\varDelta}^{(\alpha+3/2)}} \right) \\ &\simeq C_\alpha\, \mathrm{e}^{-\lambda\bar{\varDelta}^{1/2}} \left(\frac{1}{\bar{\varDelta}_s^{(\alpha+3/2)}} - \frac{1}{\bar{\varDelta}^{(\alpha+3/2)}} \right), \end{aligned} \tag{B3}$$

and accordingly,

$$\boldsymbol{T}^R_{ij} = \frac{\rho\, c_{\alpha,\lambda}}{U^3}\, C_\alpha \int_0^\infty \int_{\mathbb{R}^3 \setminus \mathcal{I}_\varDelta} (u_i - \bar{V}_i)(u_j - \bar{V}_j)\mathrm{e}^{-\lambda\bar{\varDelta}^{1/2}} \left(\frac{1}{\bar{\varDelta}_s^{(\alpha+3/2)}} - \frac{1}{\bar{\varDelta}^{(\alpha+3/2)}} \right) \mathrm{e}^{-s}\, \mathrm{d}\boldsymbol{u}\, \mathrm{d}s, \tag{B4}$$

where $c_{\alpha,\lambda}$ is a real-valued constant. As a continuous differentiable function for $\bar{\varDelta} > 1$, we proceed with the Taylor expansion of $\bar{\varDelta}_s^{-(\alpha+3/2)}$ according to

$$\bar{\varDelta}_s^{-(\alpha+3/2)} - \bar{\varDelta}^{-(\alpha+3/2)} \approx \frac{\partial \bar{\varDelta}^{-(\alpha+3/2)}}{\partial \bar{\varDelta}} (\bar{\varDelta}_s - \bar{\varDelta}) = -\left(\alpha + \frac{3}{2}\right) C_\alpha \frac{(\bar{\varDelta}_s - \bar{\varDelta})}{\bar{\varDelta}^{\alpha+5/2}}. \tag{B5}$$

In terms of the assumptions in remark 3.1, we use the same argument, presented by Samiee *et al.* (2020*a*, appendix), on approximating $\bar{\varDelta}_s - \bar{\varDelta}$ for $\bar{\varDelta} \gg 1$, which allows for $u_i - \bar{V}_i \approx u_i$ and, thus,

$$\bar{\varDelta}_s - \bar{\varDelta} \approx 2 \sum_{k=1}^{3} \frac{u_k(\bar{V}_k(\boldsymbol{x}') - \bar{V}_k(\boldsymbol{x}))}{U^2}. \tag{B6}$$

Reminding the definition of $\boldsymbol{u} = (\boldsymbol{x} - \boldsymbol{x}')/s\tau$ from § 3.2, we plug (B6) into (B4) and obtain

$$\begin{aligned} \boldsymbol{T}^R_{ij} &= (2\alpha + 3)(\rho\, c_{\alpha,\lambda}\, C_\alpha \tau^{2\alpha-1} U^{2\alpha}) \\ &\quad \times \int_0^\infty \frac{\mathrm{e}^{-s}}{s^{1-2\alpha}} \int_{\mathbb{R}^3 \setminus \mathcal{I}_\varDelta} (x_i - x_i')(x_j - x_j') \frac{(\boldsymbol{x} - \boldsymbol{x}') \boldsymbol{\cdot} (\bar{\boldsymbol{V}}(\boldsymbol{x}) - \bar{\boldsymbol{V}}(\boldsymbol{x}'))}{|\boldsymbol{x} - \boldsymbol{x}'|^{2\alpha+5} \mathrm{e}^{\lambda(|\boldsymbol{x}-\boldsymbol{x}'|/s\tau U)}}\, \mathrm{d}\boldsymbol{x}'\, \mathrm{d}s. \end{aligned} \tag{B7}$$

In order to evaluate the outer integral in (B7) and find the corresponding coefficient, our approach is to dissociate the temporal element by employing the bionomial series of

$\mathrm{e}^{\lambda(|\boldsymbol{x}-\boldsymbol{x}'|/s\tau U)}$ as

$$\begin{aligned}
\exp\left(-\frac{\lambda|\boldsymbol{x}-\boldsymbol{x}'|}{s\tau U}\right) &= \left(1-1+\exp\left(-\frac{\lambda|\boldsymbol{x}-\boldsymbol{x}'|}{s\tau U}\right)\right)^{1/s} = \sum_{k=0}^{\infty}\frac{1}{s}k\,(\exp(\bar{\lambda}|\boldsymbol{x}-\boldsymbol{x}'|)-1)\\
&= 1+\frac{1}{s}(\exp(\bar{\lambda}|\boldsymbol{x}-\boldsymbol{x}'|)-1)+\frac{\frac{1}{s}\left(\frac{1}{s}-1\right)}{2!}(\exp(\bar{\lambda}|\boldsymbol{x}-\boldsymbol{x}'|)-1)+\cdots\\
&= \sum_{k=0}^{\infty} W_{k,\infty}(s)\exp(-\bar{\lambda}_k|\boldsymbol{x}-\boldsymbol{x}'|)\\
&\simeq \sum_{k=0}^{\mathcal{K}} W_{k,\mathcal{K}}(s)\exp(-\bar{\lambda}_k|\boldsymbol{x}-\boldsymbol{x}'|),
\end{aligned} \tag{B8}$$

where $\bar{\lambda}=\lambda/\tau U$ and $\bar{\lambda}_k=\bar{\lambda}$. Under the assumption of $\lambda>0.01$, we can approximate the binomial series with the first two leading terms, which yields $W_{0,1}=1-1/s$ and $W_{1,1}=1/s$ for $\mathcal{K}=1$. Accordingly, by defining $\bar{\nu}_\alpha=(2\alpha+3)(\rho\,C_\alpha\,\tau^{2\alpha-1}U^{2\alpha})$ and

$$\bar{\phi}_k^{\mathcal{K}}(\alpha)=\int_0^\infty \frac{\mathrm{e}^{-s}}{s^{1-2\alpha}}\,W_{k,\mathcal{K}}(s)\,\mathrm{d}s, \tag{B9}$$

we obtain the closed form of $\boldsymbol{T}_{ij}^R$ as

$$\boldsymbol{T}_{ij}^R=c_{\alpha,\lambda}\,\bar{\nu}_\alpha\sum_{k=0}^{\mathcal{K}}\bar{\phi}_k^{\mathcal{K}}(\alpha)\int_{\mathbb{R}^d-B_\epsilon}\underbrace{(x_i-x_i')\,(x_j-x_j')\frac{(\boldsymbol{x}-\boldsymbol{x}')\boldsymbol{\cdot}(\bar{\boldsymbol{V}}-\bar{\boldsymbol{V}}')}{|\boldsymbol{x}-\boldsymbol{x}'|^{2\alpha+5}\mathrm{e}^{\bar{\lambda}_k|\boldsymbol{x}-\boldsymbol{x}'|}}}_{\mathcal{I}_{ij}}\,\mathrm{d}\boldsymbol{x}'. \tag{B10}$$

To ensue the proper form of the SGS stresses in the filtered NS equations, we take the derivative of $\mathcal{I}_{ij}$ term by term, which yields

$$\begin{aligned}
\frac{\partial\mathcal{I}_{ij}}{\partial x_i} = \int_{\mathbb{R}^d-B_\epsilon}\sum_{i=1}^{3}\Bigg\{&-(x_j-x_j')\frac{(\boldsymbol{x}-\boldsymbol{x}')\boldsymbol{\cdot}(\bar{\boldsymbol{V}}-\bar{\boldsymbol{V}}')}{|\boldsymbol{x}-\boldsymbol{x}'|^{2\alpha+5}\,\mathrm{e}^{\bar{\lambda}_k|\boldsymbol{x}-\boldsymbol{x}'|}}\\
&-(x_i-x_i')\,\delta_{ij}\,\frac{(\boldsymbol{x}-\boldsymbol{x}')\boldsymbol{\cdot}(\bar{\boldsymbol{V}}-\bar{\boldsymbol{V}}')}{|\boldsymbol{x}-\boldsymbol{x}'|^{2\alpha+5}\,\mathrm{e}^{\bar{\lambda}_k|\boldsymbol{x}-\boldsymbol{x}'|}}\\
&-\frac{(x_j-x_j')(x_j-x_j')(\bar{V}_i-\bar{V}_i')}{|\boldsymbol{x}-\boldsymbol{x}'|^{2\alpha+5}\,\mathrm{e}^{\bar{\lambda}_k|\boldsymbol{x}-\boldsymbol{x}'|}}\\
&-(x_i-x_i')(x_j-x_j')(x_k-x_k')\frac{\partial\bar{V}_k}{\partial x_i}\frac{\mathrm{e}^{-\bar{\lambda}_k|\boldsymbol{x}-\boldsymbol{x}'|}}{|\boldsymbol{x}-\boldsymbol{x}'|^{2\alpha+5}}\\
&(2\alpha+5)(x_i-x_i')^2(x_j-x_j')\frac{(\boldsymbol{x}-\boldsymbol{x}')\boldsymbol{\cdot}(\bar{\boldsymbol{V}}-\bar{\boldsymbol{V}}')}{|\boldsymbol{x}-\boldsymbol{x}'|^{2\alpha+5}\,\mathrm{e}^{\bar{\lambda}_k|\boldsymbol{x}-\boldsymbol{x}'|}}\\
&+\bar{\lambda}_k(x_i-x_i')(x_j-x_j')\frac{(\boldsymbol{x}-\boldsymbol{x}')\boldsymbol{\cdot}(\bar{\boldsymbol{V}}-\bar{\boldsymbol{V}}')}{|\boldsymbol{x}-\boldsymbol{x}'|^{2\alpha+5}\,\mathrm{e}^{\bar{\lambda}_k|\boldsymbol{x}-\boldsymbol{x}'|}}\Bigg\}\,\mathrm{d}\boldsymbol{x}',
\end{aligned} \tag{B11}$$

which is clearly simplified to

$$\frac{\partial \mathcal{I}_{ij}}{\partial x_i} = (\bar{\lambda}_k + 2\alpha + 5 - 3 - 1 - 1) \int_{\mathbb{R}^d - B_\epsilon} (x_j - x_j') \frac{(\boldsymbol{x} - \boldsymbol{x}') \boldsymbol{\cdot} (\bar{\boldsymbol{V}} - \bar{\boldsymbol{V}}')}{|\boldsymbol{x} - \boldsymbol{x}'|^{2\alpha+5}\, \mathrm{e}^{\bar{\lambda}_k |\boldsymbol{x} - \boldsymbol{x}'|}} \,\mathrm{d}\boldsymbol{x}'. \tag{B12}$$

Following the derivations in Samiee *et al.* (2020*a*), Epps & Cushman-Roisin (2018), (B12) can be formulated in the form of a tempered fractional Laplacian by performing the technique of integration-by-parts for (B12) as $\int A\,\mathrm{d}B = AB - \int B\,\mathrm{d}A$. We consider

$$A = (x_j - x_j')(\bar{V}_k - \bar{V}_k')\,\mathrm{e}^{-\bar{\lambda}_k |\boldsymbol{x} - \boldsymbol{x}'|}, \quad \mathrm{d}B = \frac{(x_k - x_k')}{|\boldsymbol{x} - \boldsymbol{x}'|^{2\alpha+5}}\,\mathrm{d}\boldsymbol{x}', \tag{B13a,b}$$

which directly leads to $AB|_{u\in\mathbb{R}^3} \simeq 0$. Therefore, we get $\int A\,\mathrm{d}B = -\int B\,\mathrm{d}A$, in which

$$\left.\begin{aligned} B &= \frac{-1}{(2\alpha+3)|\boldsymbol{x} - \boldsymbol{x}'|^{2\alpha+3}}, \\ \mathrm{d}A &= \delta_{jk}(\bar{V}_k - \bar{V}_k')\mathrm{e}^{-\bar{\lambda}_k |\boldsymbol{x} - \boldsymbol{x}'|} + (x_j - x_j')\left(\frac{\partial \bar{V}_k}{\partial x_k}\right)\mathrm{e}^{-\bar{\lambda}_k |\boldsymbol{x} - \boldsymbol{x}'|} \\ &\quad - \bar{\lambda}_k (x_j - x_j')(\bar{V}_k - \bar{V}_k')\mathrm{e}^{-\bar{\lambda}_k |\boldsymbol{x} - \boldsymbol{x}'|}\,\mathrm{d}\boldsymbol{x}'. \end{aligned}\right\} \tag{B14}$$

We can make even more simplifications by eliminating the second term of dA due to the incompressibility assumption, i.e. $\partial \bar{V}_k/\partial x_k = 0$. Moreover, by evaluating $\int B\,\mathrm{d}A$ the last term vanishes since it represents an odd function of $\boldsymbol{x}'$. Therefore, the ultimate form of the TFSGS model is found to be

$$\begin{aligned} (\boldsymbol{\nabla} \boldsymbol{\cdot} \boldsymbol{T}^{\mathcal{R}})_j &= c_{\alpha,\lambda}\, \bar{\nu}_\alpha \sum_{k=0}^{\mathcal{K}} \frac{(2\alpha + \bar{\lambda}_k)}{(2\alpha+3)}\, \bar{\phi}_k^{\mathcal{K}}(\alpha) \int_{\mathbb{R}^d - B_\epsilon} \frac{(\bar{V}_j - \bar{V}_j')}{|\boldsymbol{x} - \boldsymbol{x}'|^{2\alpha+3}\, \mathrm{e}^{\bar{\lambda}_k |\boldsymbol{x} - \boldsymbol{x}'|}}\,\mathrm{d}\boldsymbol{x}', \\ &= \nu_\alpha \sum_{k=0}^{\mathcal{K}} \phi_k^{\mathcal{K}}(\alpha, \bar{\lambda}_k)(\varDelta + \bar{\lambda}_k)^\alpha\, \bar{V}_j, \end{aligned} \tag{B15}$$

where $\nu_\alpha = \mathrm{c}_{\alpha,\lambda}\,\bar{\nu}_\alpha$.

REFERENCES

AKHAVAN-SAFAEI, A., SAMIEE, M. & ZAYERNOURI, M. 2021 Data-driven fractional subgrid-scale modeling for scalar turbulence: a nonlocal LES approach. *J. Comput. Phys.* **446**, 110571.

AKHAVAN-SAFAEI, A., SEYEDI, S.H. & ZAYERNOURI, M. 2020 Anomalous features in internal cylinder flow instabilities subject to uncertain rotational effects. *Phys. Fluids* **32** (9), 094107.

AKHAVAN-SAFAEI, A. & ZAYERNOURI, M. 2020 A parallel integrated computational-statistical platform for turbulent transport phenomena. arXiv:2012.04838.

BECK, A. & KURZ, M. 2020 A perspective on machine learning methods in turbulence modelling. arXiv:2010.12226.

BOUFFANAIS, R. 2010 Advances and challenges of applied large-eddy simulation. *Comput. Fluids* **39** (5), 735–738.

BRIARD, A., GOMEZ, T. & CAMBON, C. 2016 Spectral modelling for passive scalar dynamics in homogeneous anisotropic turbulence. *J. Fluid Mech.* **799**, 159–199.

BUARIA, D., PUMIR, A. & BODENSCHATZ, E. 2020 Self-attenuation of extreme events in Navier–Stokes turbulence. *Nat. Commun.* **11** (1), 5852.

BURKOVSKA, O., GLUSA, C. & D'ELIA, M. 2020 An optimization-based approach to parameter learning for fractional type nonlocal models. arXiv:2010.03666.

BURTON, G.C. & DAHM, W.J.A. 2005 Multifractal subgrid-scale modeling for large-eddy simulation. II. Backscatter limiting and a posteriori evaluation. *Phys. Fluids* **17** (7), 075112.

Cairoli, A. 2016 Towards a comprehensive framework for the analysis of anomalous diffusive systems. PhD thesis, Queen Mary University of London.

Cambon, C. & Scott, J.F. 1999 Linear and nonlinear models of anisotropic turbulence. *Annu. Rev. Fluid Mech.* **31** (1), 1–53.

Cerutti, S., Meneveau, C. & Knio, O.M. 2000 Spectral and hyper eddy viscosity in high-Reynolds-number turbulence. *J. Fluid Mech.* **421**, 307–338.

Chao, M.A., Kulkarni, C., Goebel, K. & Fink, O. 2020 Fusing physics-based and deep learning models for prognostics. arXiv:2003.00732.

Chen, H., Orszag, S.A., Staroselsky, I. & Succi, S. 2004 Expanded analogy between Boltzmann kinetic theory of fluids and turbulence. *J. Fluid Mech.* **519**, 301–314.

Deng, W., Li, B., Tian, W. & Zhang, P. 2018 Boundary problems for the fractional and tempered fractional operators. *Multiscale Model. Simul.* **16** (1), 125–149.

Di Leoni, P.C., Zaki, T.A., Karniadakis, G. & Meneveau, C. 2020 Two-point stress-strain rate correlation structure and non-local eddy viscosity in turbulent flows. arXiv:2006.02280.

Di Nezza, E., Palatucci, G. & Valdinoci, E. 2012 Hitchhiker's guide to the fractional Sobolev spaces. *Bull. Sci. Mathématiques* **136** (5), 521–573.

Egolf, P.W. & Hutter, K. 2017 Fractional turbulence models. In *Progress in Turbulence VII*, pp. 123–131.

Egolf, P.W. & Hutter, K. 2020 *Nonlinear, Nonlocal and Fractional Turbulence*, Graduate Studies in Mathematics. Springer.

Epps, B.P. & Cushman-Roisin, B. 2018 Turbulence modeling via the fractional Laplacian. arXiv:1803.05286.

Evin, G., Blanchet, J., Paquet, E., Garavaglia, F. & Penot, D. 2016 A regional model for extreme rainfall based on weather patterns subsampling. *J. Hydrol.* **541**, 1185–1198.

Girimaji, S.S. 2007 Boltzmann kinetic equation for filtered fluid turbulence. *Phys. Rev. Lett.* **99** (3), 034501.

Hamlington, P.E. & Dahm, W.J.A. 2008 Reynolds stress closure for nonequilibrium effects in turbulent flows. *Phys. Fluids* **20** (11), 115101.

Henderson, D.W. & Taimina, D. 2000 *Experiencing Geometry*. Prentice Hall.

Hill, R.J. 2002 Exact second-order structure-function relationships. *J. Fluid Mech.* **468**, 317–326.

Holgate, J., Skillen, A., Craft, T. & Revell, A. 2019 A review of embedded large eddy simulation for internal flows. *Arch. Comput. Methods Engng* **26** (4), 865–882.

Huang, L. 2015 Density estimates for SDEs driven by tempered stable processes. arXiv:1504.04183.

Ionescu, C., Lopes, A., Copot, D., Machado, J.A.T. & Bates, J.H.T. 2017 The role of fractional calculus in modeling biological phenomena: a review. *Commun. Nonlinear Sci. Numer. Simul.* **51**, 141–159.

Jacob, J., Malaspinas, O. & Sagaut, P. 2018 A new hybrid recursive regularised Bhatnagar–Gross–Krook collision model for Lattice Boltzmann method-based large eddy simulation. *J. Turbul.* **19** (11–12), 1051–1076.

Jin, G., Wang, S., Wang, Y. & He, G. 2018 Lattice Boltzmann simulations of high-order statistics in isotropic turbulent flows. *Z. Angew. Math. Mech.* **39** (1), 21–30.

Jouybari, M.A., Yuan, J., Brereton, G.J. & Murillo, M.S. 2020 Data-driven prediction of the equivalent sand-grain height in rough-wall turbulent flows. arXiv:2002.01515.

Kaleta, K. & Sztonyk, P. 2015 Estimates of transition densities and their derivatives for jump Lévy processes. *J. Math. Anal. Appl.* **431** (1), 260–282.

Kassinos, S.C., Reynolds, W.C. & Rogers, M.M. 2001 One-point turbulence structure tensors. *J. Fluid Mech.* **428**, 213–248.

Kharazmi, E. & Zayernouri, M. 2019 Fractional sensitivity equation method: application to fractional model construction. *J. Sci. Comput.* **80** (1), 110–140.

Kurz, M. & Beck, A. 2020 A machine learning framework for LES closure terms. arXiv:2010.03030.

Laval, J.P., Dubrulle, B. & Nazarenko, S. 2001 Nonlocality and intermittency in three-dimensional turbulence. *Phys. Fluids* **13** (7), 1995–2012.

Malaspinas, O. & Sagaut, P. 2012 Consistent subgrid scale modelling for lattice Boltzmann methods. *J. Fluid Mech.* **700**, 514–542.

Meneveau, C. 1994 Statistics of turbulence subgrid-scale stresses: necessary conditions and experimental tests. *Phys. Fluids* **6** (2), 815–833.

Meral, F.C., Royston, T.J. & Magin, R. 2010 Fractional calculus in viscoelasticity: an experimental study. *Commun. Nonlinear Sci. Numer. Simul.* **15** (4), 939–945.

Mishra, A.A. & Girimaji, S. 2019 Linear analysis of non-local physics in homogeneous turbulent flows. *Phys. Fluids* **31** (3), 035102.

Mishra, A.A. & Girimaji, S.S. 2017 Toward approximating non-local dynamics in single-point pressure–strain correlation closures. *J. Fluid Mech.* **811**, 168–188.

MORTENSEN, M. & LANGTANGEN, H.P. 2016 High performance python for direct numerical simulations of turbulent flows. *Comput. Phys. Commun.* **203**, 53–65.

MOSER, R.D., HAERING, S.W. & YALLA, G.R. 2021 Statistical properties of subgrid-scale turbulence models. *Annu. Rev. Fluid Mech.* **53**, 255–286.

NAGHIBOLHOSSEINI, M. & LONG, G.R. 2018 Fractional-order modelling and simulation of human ear. *Intl J. Comput. Maths* **95** (6–7), 1257–1273.

PANG, G., D'ELIA, M., PARKS, M. & KARNIADAKIS, G.E. 2020 nPINNs: nonlocal physics-informed neural networks for a parametrized nonlocal universal Laplacian operator. Algorithms and applications. *J. Comput. Phys.* **422**, 109760.

PATRA, A.K., BEVILACQUA, A. & SAFAEI, A.A. 2018 Analyzing complex models using data and statistics. In *International Conference on Computational Science*, pp. 724–736. Springer.

PAWAR, S., SAN, O., RASHEED, A. & VEDULA, P. 2020 A priori analysis on deep learning of subgrid-scale parameterizations for Kraichnan turbulence. *Theor. Comput. Fluid Dyn.* **34** (4), 429–455.

PIOMELLI, U. 2014 Large eddy simulations in 2030 and beyond. *Phil. Trans. R. Soc. Lond.* A **372** (2022), 20130320.

POPE, S.B. 2000 *Turbulent Flows*. Cambridge University Press.

PORTWOOD, G.D., NADIGA, B.T., SAENZ, J.A. & LIVESCU, D. 2021 Interpreting neural network models of residual scalar flux. *J. Fluid Mech.* **907**, A23.

PREMNATH, K.N., PATTISON, M.J. & BANERJEE, S. 2009 Dynamic subgrid scale modeling of turbulent flows using lattice-Boltzmann method. *Physica* A*: Stat. Mech. Applics.* **388** (13), 2640–2658.

SABZIKAR, F., MEERSCHAERT, M.M. & CHEN, J. 2015 Tempered fractional calculus. *J. Comput. Phys.* **293**, 14–28.

SAGAUT, P. 2010 Toward advanced subgrid models for Lattice-Boltzmann-based large-eddy simulation: theoretical formulations. *Comput. Maths Applics.* **59** (7), 2194–2199.

SAGAUT, P. & CAMBON, C. 2008 *Homogeneous Turbulence Dynamics*, vol. 10. Springer.

SAMIEE, M. 2021 *Data-Infused Fractional Modeling and Spectral Numerical Analysis for Anomalous Transport and Turbulence*. Michigan State University.

SAMIEE, M., AKHAVAN-SAFAEI, A. & ZAYERNOURI, M. 2020*a* A fractional subgrid-scale model for turbulent flows: theoretical formulation and a priori study. *Phys. Fluids* **32** (5), 055102.

SAMIEE, M., KHARAZMI, E., MEERSCHAERT, M.M. & ZAYERNOURI, M. 2020*b* A unified Petrov–Galerkin spectral method and fast solver for distributed-order partial differential equations. *Commun. Appl. Math. Comput.* **3**, 61–90.

SAMIEE, M., ZAYERNOURI, M. & MEERSCHAERT, M.M. 2019 A unified spectral method for FPDEs with two-sided derivatives; part I: a fast solver. *J. Comput. Phys.* **385**, 225–243.

SHE, Z.-S., JACKSON, E. & ORSZAG, S.A. 1990 Intermittent vortex structures in homogeneous isotropic turbulence. *Nature* **344** (6263), 226–228.

SHIVAMOGGI, B.K. & TUOVILA, N. 2019 Direct interaction approximation for non-Markovianized stochastic models in the turbulence problem. *Chaos* **29** (6), 063124.

SIRIGNANO, J., MACART, J.F. & FREUND, J.B. 2020 DPM: a deep learning PDE augmentation method with application to large-eddy simulation. *J. Comput. Phys.* **423**, 109811.

SMAGORINSKY, J. 1963 General circulation experiments with the primitive equations: I. The basic experiment. *Mon. Weath. Rev.* **91** (3), 99–164.

SOTO, R. 2016 *Kinetic Theory and Transport Phenomena*, vol. 25. Oxford University Press.

STEIN, E.M. 1970 *Singular Integrals and Differentiability Properties of Functions*, vol. 2. Princeton University Press.

SUZUKI, J., ZHOU, Y., D'ELIA, M. & ZAYERNOURI, M. 2021*a* A thermodynamically consistent fractional visco-elasto-plastic model with memory-dependent damage for anomalous materials. *Comput. Meth. Appl. Mech. Engng* **373**, 113494.

SUZUKI, J.L., KHARAZMI, E., VARGHAEI, P., NAGHIBOLHOSSEINI, M. & ZAYERNOURI, M. 2021*b* Anomalous nonlinear dynamics behavior of fractional viscoelastic beams. *J. Comput. Nonlinear Dyn.* **16** (11), 111005.

SUZUKI, J.L. & ZAYERNOURI, M. 2021 A self-singularity-capturing scheme for fractional differential equations. *Intl J. Comput. Maths* **98** (5), 933–960.

TAGHIZADEH, S., WITHERDEN, F.D. & GIRIMAJI, S.S. 2020 Turbulence closure modeling with data-driven techniques: physical compatibility and consistency considerations. *New J. Phys.* **22** (9), 093023.

VINCENT, A. & MENEGUZZI, M. 1991 The spatial structure and statistical properties of homogeneous turbulence. *J. Fluid Mech.* **225**, 1–20.

WERON, R. 2001 Levy-stable distributions revisited: tail index > 2 does not exclude the Levy-stable regime. *Intl J. Mod. Phys. C* **12** (02), 209–223.

WILLARD, J., JIA, X., XU, S., STEINBACH, M. & KUMAR, V. 2020 Integrating physics-based modeling with machine learning: a survey. arXiv:2003.04919.

XIE, C. & FANG, S. 2019 A second-order finite difference method for fractional diffusion equation with Dirichlet and fractional boundary conditions. *Numer. Meth. Partial Differ. Equ.* **35** (4), 1383–1395.

YANG, X.I.A. & LOZANO-DURÁN, A. 2017 A multifractal model for the momentum transfer process in wall-bounded flows. *J. Fluid Mech.* **824**, R2.

YOU, H., YU, Y., TRASK, N., GULIAN, M. & D'ELIA, M. 2021 Data-driven learning of nonlocal physics from high-fidelity synthetic data. *Comput. Meth. Appl. Mech. Engng* **374**, 113553.

ZAKY, M.A., HENDY, A.S. & MACÍAS-DÍAZ, J.E. 2020 Semi-implicit Galerkin–Legendre spectral schemes for nonlinear time-space fractional diffusion–reaction equations with smooth and nonsmooth solutions. *J. Sci. Comput.* **82** (1), 13.

ZAYERNOURI, M., AINSWORTH, M. & KARNIADAKIS, G.EM. 2015 Tempered fractional Sturm–Liouville eigenproblems. *SIAM J. Sci. Comput.* **37** (4), A1777–A1800.

ZHANG, Z., DENG, W. & KARNIADAKIS, G.EM. 2018 A Riesz basis Galerkin method for the tempered fractional Laplacian. *SIAM J. Numer. Anal.* **56** (5), 3010–3039.

ZHIYIN, Y. 2015 Large-eddy simulation: past, present and the future. *Chin. J. Aeronaut.* **28** (1), 11–24.